Chemical Engineering Journal 530 (2026) 173135

Contents lists available at ScienceDirect

Chemical Engineering Journal

journal homepage: www.elsevier.com/locate/cej

One-step synthesis of redox-active benzoquinone polymer dots for supercapacitor energy storage

Shimaa Abdelnaser [a,b], Yousra M. Nabil [a,b], Hira Karim [c], Shiao-Wei Kuo [a], Ahmed F.M. EL-Mahdy [a,b,*]

[a] Department of Materials and Optoelectronic Science, National Sun Yat-Sen University, Kaohsiung 80424, Taiwan
[b] Chemistry Department, Faculty of Science, Assiut University, Assiut 71516, Egypt
[c] Department of Chemistry, School of Natural Sciences (SNS), National University of Sciences and Technology (NUST), H-12, Islamabad 44000, Pakistan

ARTICLE INFO

Keywords:
Benzoquinone
Redox active
Polymer dots
Tröger base
Supercapacitors

ABSTRACT

Polymer dots (PDs) combine the structural versatility of polymers with the electrochemical features of nanoparticles, offering promise for energy storage. However, their poor conductivity and limited redox-active sites restrict capacitance and long-term cycling stability. Herein, we report the one-step synthesis of benzoquinone-based PDs (BQ-PDs) using p-benzoquinone (BQ) and aromatic diamines: 2,8-dimethyl-Tröger's base diamine (Tg-2NH_2, Tg) and 2,4-diaminotoluene (To-2NH_2, To). This direct approach eliminates the need for separate polymerization and nanoprecipitation, yielding nanoscale PDs (45–80 nm) with abundant carbonyl functionalities and excellent thermal stability (T_{d10} = 387.04 °C for BQ-Tg, 380.95 °C for BQ-To). Integration of BQ units with Tg or To linkers imparts efficient charge transport and pseudocapacitive behavior. BQ-Tg PDs deliver a specific capacitance of 268.8 F g^{-1} at 0.5 A g^{-1} with 79.3% retention after 10,000 cycles in a three-electrode supercapacitor system. After 6000 cycles in a symmetric two-electrode supercapacitor at 2.2 A g^{-1}, the BQ-Tg polymer retained a capacitance of 105.29 F g^{-1} with 88.34% capacity retention, delivering an energy density of 14.63 Wh kg^{-1} at a power density of 555.8 W kg^{-1}. This work demonstrates a simple molecular design strategy for redox-active quinone PDs as lightweight, stable, and good performance electrode materials for next-generation supercapacitors.

1. Introduction

Global energy demand spans transportation, industry, residential, and commercial sectors and continues to rise with population growth and economic development. Meanwhile, heavy reliance on fossil fuels causes environmental and financial challenges, motivating a shift toward renewable energy [1,2]. Because renewables are intermittent, efficient energy-storage technologies—such as batteries and supercapacitors—are essential to balance supply and demand [3]. Supercapacitors (SCs), also known as electrochemical capacitors, are promising energy-storage devices because they deliver high power density, fast charge–discharge, long cycle life, low cost, and lightweight features [4–6]. SCs are typically classified as electric double-layer capacitors (EDLCs) or pseudocapacitors: EDLCs store charge via ion adsorption at the electrode/electrolyte interface (often using carbon materials), whereas pseudocapacitors rely on fast Faradaic reactions (commonly enabled by conducting polymers) [7–10]. In this context, polymer-based electrodes are particularly appealing due to their low density, high structural tunability, and the ability to incorporate abundant functional/redox-active groups that contribute to pseudocapacitive charge storage [8,11,12]. Moreover, polymer chemistry enables molecular-level design of ion-accessible architectures and tailored interfacial wettability, which can enhance charge/ion transport [11,13]. Importantly, scalable deployment also requires cost-effective precursors and simple, one-pot synthesis routes that reduce processing steps, time, and manufacturing cost. However, many polymer electrodes still face challenges such as limited conductivity and incomplete utilization of redox sites, motivating nanoscale polymer engineering strategies such as polymer dots.

Polymer dots (PDs) are quantum dots that exhibit characteristics of both quantum dots and polymers [14]. PDs are nanostructures formed by the bending and folding of polymer chains to create nanoparticles, which typically contain more than half of their volume as conjugated polymer [15]. In simple terms, the conjugated polymer is the main

* Corresponding author at: Department of Materials and Optoelectronic Science, National Sun Yat-Sen University, Kaohsiung 80424, Taiwan.
E-mail address: ahmedelmahdy@mail.nsysu.edu.tw (A.F.M. EL-Mahdy).

https://doi.org/10.1016/j.cej.2026.173135
Received 13 October 2025; Received in revised form 3 January 2026; Accepted 16 January 2026
Available online 17 January 2026

component of PDs and greatly affects their properties. The conjugated architecture in PDs plays a crucial role in determining their optical, electronic, and electrochemical behaviors [16]. Extensive π-conjugation across the polymer backbone facilitates effective charge transport and electron delocalization, thereby enhancing electronic conductivity [17,18]. This property is crucial for applications in optoelectronics and energy storage technologies. In addition, the heteroatom-containing functional groups (e.g., C═O, C═N, N–O/N═O, –NH/–NH_2, and C—O) can modulate the properties of polymer dots [15,19]. Due to their many functional groups and conjugated structures, these polymers enhance ion mobility and provide additional sites for charge storage [17,20]. Consequently, they serve as attractive candidates for the construction of polymer dots infused with various functional groups. Due to their diminutive size, inexpensive, non-toxic, good at conducting electricity, and efficient transfer of charged particles via electron stimulation, they are great alternatives for a lot of technical uses like chemical sensing, photocatalysis, bioimaging, drug delivery, and energy storage [21–25]. Also, integrating heteroatoms is an efficacious approach for boosting the pseudo-capacitance of carbon electrodes· [26]. Incorporating heteroatoms like S, N, B, and P into the carbon nanostructures not only makes them more pseudocapacitive, but it also makes the carbon-based electrode more wettable to aqueous solutions, thus enhancing the capacitance [27,28]. The nanostructure and conjugated polymer networks in PDs provide superior electrical conductivity, facilitating efficient electron transfer and minimal internal resistance during charge-discharge cycles [15,29]. Moreover, PDs demonstrate good chemical and thermal stability, crucial for sustained cycling performance and operational dependability [15,16,24]. These properties collectively render PDs exceptionally appealing for sophisticated supercapacitor applications.

Tröger's base (Tg) was first reported by Julius Tröger in 1887 and has attracted enduring interest due to its rigid V-shaped scaffold and C_2 chirality [30–33]. Tröger's base and its derivatives remain widely studied for their roles in supramolecular assembly, enantioselective recognition/separation, and molecular replication [34]. Additionally, polymers derived from Tröger's base are often classified as polymers of intrinsic microporosity (PIMs) because the monomer's rigid V-shaped structure generates intrinsic free volume and permanent microporosity [35–38]. To our knowledge, Tg-derived polymers have been used as supercapacitor carbon precursors via high-temperature carbonization (e.g., 1100 °C) to produce carbon electrodes [39]. In contrast, Tg-derived polymer dots incorporating electrochemically redox-active moieties for energy storage have not yet been reported. On the other hand, *p*-benzoquinone (BQ), which possesses two carbonyl groups, participates in a reversible faradaic redox reaction that entails the transfer of two electrons and two protons [40]. BQ and its derivatives have garnered interest as a novel category of electrode materials for supercapacitors, due to their sustainable characteristics, adaptable molecular architecture, and superior ability for quick multi-electron redox reactions [41]. Because BQs have a smaller molecular size than many other quinones, they are expected to offer higher theoretical specific capacity and faster redox kinetics, enabling improved energy and power densities [42]. Despite their advantages, using BQs as redox-active materials is often limited by poor cycling stability, limited utilization of active sites, and inadequate chemical stability (partly due to their relatively low aromatic stabilization) [42,43]. A common strategy is to immobilize BQs within carbon matrices or polymer frameworks to suppress dissolution while enhancing chemical stability and maintaining accessible redox-active sites [43,44].

In previous studies, the preparation of PDs typically required a two-step approach. First, small organic monomers were polymerized to form bulk polymer chains. Subsequently, these polymers were converted into nanoscale particles through a nanoprecipitation process. Although effective, this multi-step route is relatively time-consuming and involves additional solvents and processing, which can limit efficiency, scalability, and control over the final PD properties (Scheme 1a) [15,16]. In our study, we developed a novel series of benzoquinone-based polymer dots (BQ-PDs) through a simple one-step reaction between p-benzoquinone (BQ) and aromatic diamines: 2,8-Dimethyl-6H,12H-5,11-methanodibenzo[b,f][1,5]diazocine-3,9-diamine (Tröger's base diamine, Tg-2NH_2) and 2,4-diaminotoluene (To-2NH_2) (Scheme 1b). Using Tg-2NH_2 (Scheme S1) with BQ in ethanol afforded the BQ-Tg polymer dots (BQ-Tg PDs) (Schemes 1b and S2), while To-2NH_2 with BQ yielded the BQ-To polymer dots (BQ-To PDs) (Schemes 1b and S3). This direct approach eliminates the need for separate polymerization and nanoprecipitation, producing nanoscale PDs with uniformly distributed redox-active BQ

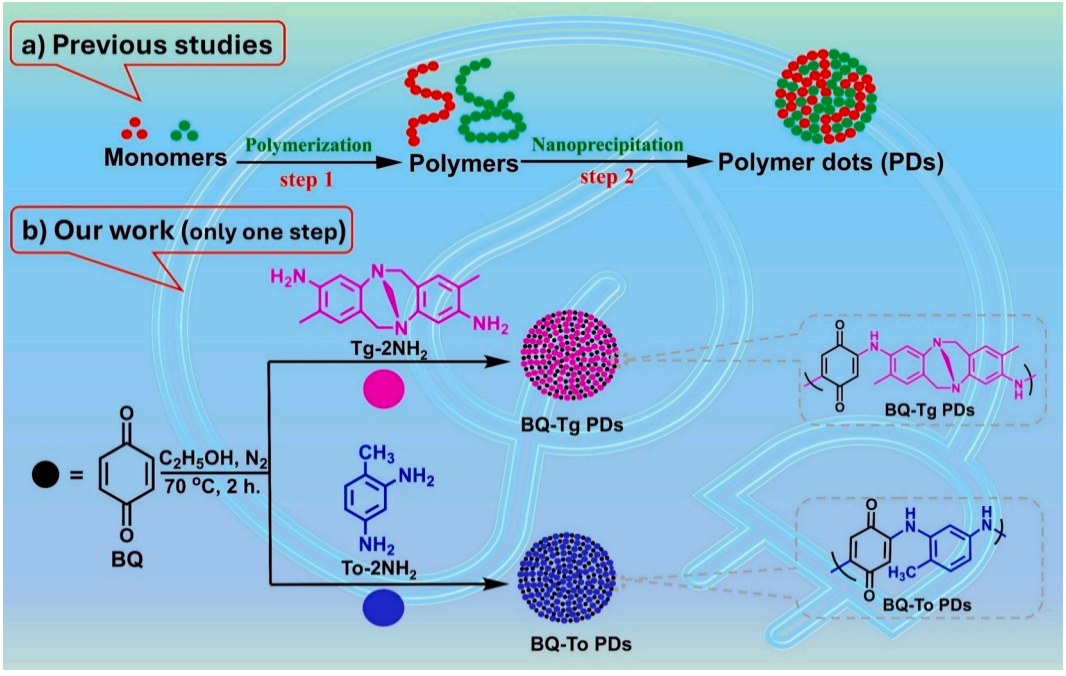

Scheme 1. Synthetic strategy for benzoquinone-based polymer dots (BQ-PDs). (a) The conventional two-step method involves the polymerization of monomers followed by nanoprecipitation to form polymer dots. (b) One-step synthesis of BQ-Tg and BQ-To polymer dots via direct reaction of BQ with Tg-2NH_2 or To-2NH_2.

units embedded in the framework. The resulting BQ-Tg and BQ-To PDs exhibit structural stability, abundant electroactive sites, and enhanced charge transport, making them promising candidates for good-performance energy storage. It is noteworthy that both BQ-Tg and BQ-To PDs show high thermal stability; the BQ-Tg polymer achieved a T_{d10} equal to 387.04 °C and a char yield surpassing 58.41%, while the BQ-To had 380.95 °C and 57.18%. Additionally, the synthesized BQ-PDs show pseudocapacitive qualities and a notable specific capacity higher than other reported polymers. In a three-electrode setup, the BQ-Tg polymer possesses a specific capacitance of 268.77 F g^{-1} with a current density of 0.5 A g^{-1} and holds 79.3% of its beginning capacitance following 10,000 charge-discharge cycles. Furthermore, when tested in a two-electrode device, it indicates a specific capacitance of 105.29 F g^{-1}, maintaining a retention of 88.34% after 6000 cycles. Finally, redox-active BQ-based PDs can be efficiently utilized in the fabrication of each of the symmetric two-electrode and three-electrode capacitor systems, facilitating effective energy storage performance.

2. Experimental

2.1. Materials

Formaldehyde (37% in H_2O) and sulfuric acid were purchased from Sigma-Aldrich. p-Benzoquinone (98%) was sourced from Thermo Scientific. 2,4-Diaminotoluene from the Tokyo Chemical Industry (TCI). Supporting Information (Section S1. Materials) provides a comprehensive account of the supplementary reagents and materials utilized in polymer synthesis.

2.2. Preparation of BQ-Tg polymer dots

First, a two-necked flask (50 mL) was charged with Tröger's Base, Tg-$2NH_2$ (280.17 mg, 1 mmol) and evacuated for 15 min under vacuum. Next, a solution of p-benzoquinone in ethanol (324.06 mg, 3 mmol, 20 mL) was added under stirring in a nitrogen atmosphere. The mixture was then stirred for two hours at 70 °C. When cooled to room temperature, it was filtered and washed three times with ethyl acetate. Finally, the products were separated and vacuum-dried for 24 h at 60 °C to obtain a dark brown solid yield of 51.4% (Scheme S2).

2.3. Preparation of BQ-To polymer dots

First, a two-necked flask (50 mL) was charged with 2,4-diaminotoluene, To-$2NH_2$ (122.17 mg, 1 mmol), and evacuated for 15 min under vacuum. Then, a solution of p-benzoquinone in ethanol (324.06 mg, 3 mmol, 20 mL) was added while stirring under a nitrogen atmosphere. The mixture was stirred for two hours at 70 °C. After cooling to room temperature, it was filtered and washed three times with ethyl acetate. Finally, the product was separated and vacuum-dried for 24 h at 60 °C, yielding a black solid with a 47.06% yield (Scheme S3).

3. Results and discussion

3.1. The synthesis and characterization of compounds

The synthesis of benzoquinone-based polymer dots (BQ-PDs) was achieved through a straightforward one-step condensation reaction between p-benzoquinone (BQ) and aromatic diamines. For the BQ-Tg PDs, 2,8-dimethyl-6H,12H-5,11-methanodibenzo[b,f][1,5] diazocine-3,9-diamine (Tg-$2NH_2$) (Scheme S1 and Figs. S1-S4) reacted with BQ in ethanol under a nitrogen atmosphere at 70 °C for 2 h (Schemes 1b and S2). The molecular ion M + 1 peak was detected in the mass spectrum of the Tg-$2NH_2$ monomer at *m/z* 281.17 (Fig. S4). The diamine units provided by the rigid Tröger's base structure facilitated the formation of nanoscale polymeric dots enriched with redox-active benzoquinone moieties. Similarly, for the BQ-To PDs, 2,4-diaminotoluene (To-$2NH_2$) was reacted with BQ under the same conditions, yielding uniform PDs with integrated benzoquinone functionalities (Schemes 1b and S3). The molecular ion M + 1 peak was observed in the mass spectrum of the To-$2NH_2$ monomer at m/z 123.09 (Fig. S5). This approach bypasses the conventional two-step polymerization and nanoprecipitation route, directly producing nanoscale BQ-Tg and BQ-To PDs with well-distributed active sites. The resulting materials combine structural rigidity, abundant electroactive carbonyl groups, and stable aromatic frameworks, making them highly suitable for efficient charge storage in supercapacitor applications. The successful formation of BQ-Tg and BQ-To polymer dots was confirmed by FT-IR spectroscopy (Figs. 1a and 1b). In the spectra of the precursor diamines (Tg-$2NH_2$ and To-$2NH_2$), the broad N—H stretching vibrations of the primary amine groups appeared in the regions 3550–3246 cm^{-1} and 3460–3220 cm^{-1}, respectively. Notably, these characteristic –NH_2 absorptions completely disappeared in the spectra of the corresponding BQ-Tg and BQ-To PDs, indicating full consumption of the amine groups during polymerization. Instead, new bands corresponding to secondary –NH stretching were observed at 3570–3166 cm^{-1} for BQ-Tg PDs and 3544–3155 cm^{-1} for BQ-To PDs, confirming the formation of imine-type linkages. Both polymers also displayed C—H aromatic stretching near 3019 cm^{-1} (BQ-Tg PDs) and 3033 cm^{-1} (BQ-To PDs), as well as distinct carbonyl (C=O) stretching vibrations at 1622 and 1629 cm^{-1}, respectively. These peaks are slightly shifted compared to the starting monomers, further verifying the successful integration of benzoquinone units into the polymer framework. Collectively, the disappearance of amine stretches and the appearance of new NH and C=O vibrations provide strong evidence for the successful synthesis of BQ-based polymer dots.

The chemical structures of the synthesized polymer dots were further confirmed by ^{1}H NMR and ^{13}C NMR (Figs. S6-S9). For the BQ-Tg PDs (Figs. S6 and S7), the ^{1}H NMR spectrum displayed a singlet at δ 7.43 corresponding to the NH proton, while the multiplet between δ 7.06–6.44 is assigned to aromatic protons. Additional signals at δ 4.56 and 4.00 (singlets, CH_2 groups a and c), δ 4.25 (singlet, N–CH_2–N), and δ 2.04 (singlet, CH_3 group) confirmed the incorporation of the Tröger's base diamine. The ^{13}C NMR spectrum showed a resonance at δ 143.62 for the carbonyl (C=O) group, signals in the range δ 131–106 corresponding to aromatic carbons, and peaks at δ 59.5 (CH_2-a), 38.14 (CH_2-b), and 16.44 (CH_3), consistent with the expected structure. Similarly, for the BQ-To PDs (Figs. S8 and S9), the ^{1}H NMR spectrum exhibited a singlet at δ 8.05 for NH, a multiplet at δ 7.06–6.10 for aromatic protons, and a singlet at δ 2.04 corresponding to the CH_3 group. The ^{13}C NMR spectrum revealed a peak at δ 145.55 assigned to the carbonyl carbon, resonances in the range δ 129–109 for aromatic carbons, and a signal at δ 16.85 for the methyl group. These spectra confirm the successful formation of BQ-Tg and BQ-To PDs with the expected structural motifs. Notably, BQ-Tg and BQ-To are polymer dots that exist as nanoparticle aggregates comprising many polymer chains/segments; therefore, they do not possess a definable single-chain molecular weight, and intact-mass determination by MALDI-TOF is not meaningful for these assemblies. In addition, attempts to determine molecular weight by GPC/SEC were unsuccessful because the polymer dots do not undergo molecular dissolution and may exhibit aggregation/retention behavior during chromatographic separation. Instead, an appropriate descriptor is the molar mass per particle (particle molecular weight), which can be estimated from the DLS hydrodynamic diameter using eq. S1. Using the DLS mean diameters (~58 nm for BQ-Tg and ~ 72 nm for BQ-To), the estimated particle molar masses were (6.8–8.0) × 10^7 g mol^{-1} (68–80 MDa) for BQ-Tg and (1.29–1.53) × 108 g mol^{-1} (129–153 MDa) for BQ-To.

TGA indicated that the redox-active PDs studied exhibited a substantial extent of thermal stability (Fig. 1c and Table S1). BQ-Tg PDs showed high thermal stability, with a 10% weight-loss temperature (T_{d10}%) of 387.04 °C, slightly higher than that of BQ-To PDs (380.95 °C). Additionally, TGA analysis indicated that the char yield values for the BQ-Tg and BQ-To PDs were estimated at 58.41% and 57.18%, respectively. PDs typically decompose at elevated

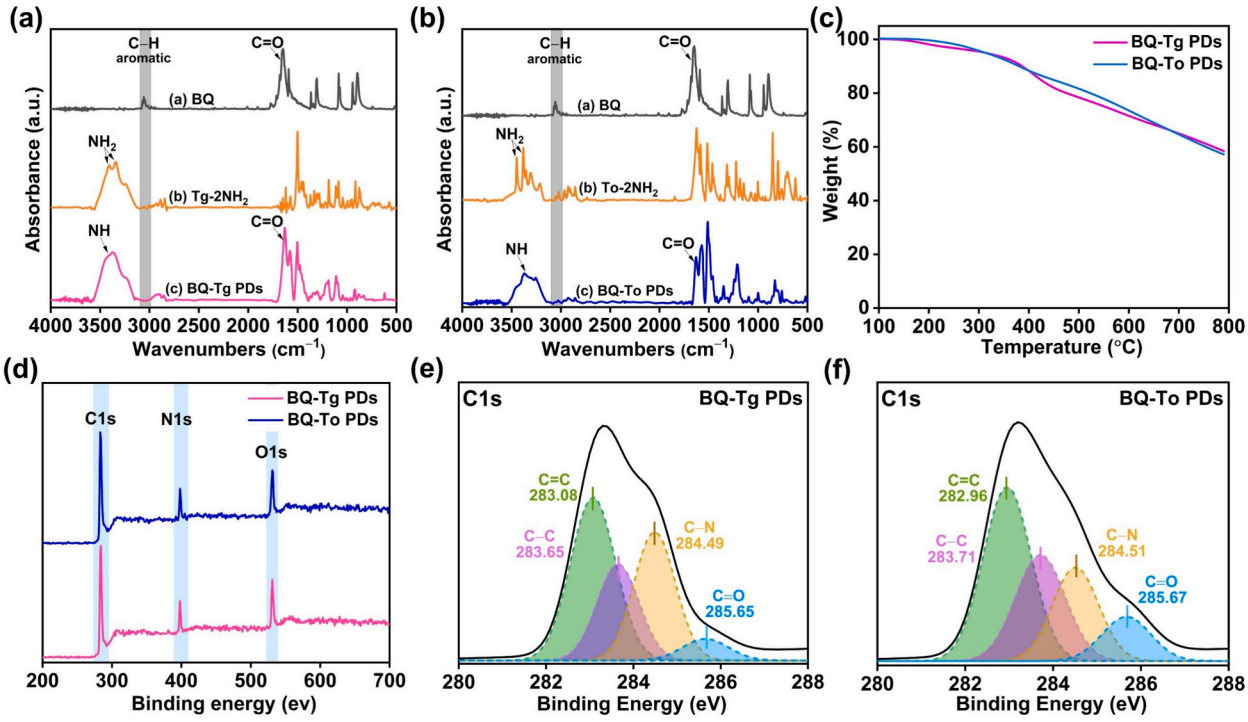

Fig. 1. (a,b) FT-IR spectra of (a) BQ-Tg PDs and the corresponding monomers. (b) BQ-To PDs and the corresponding monomers. (c) TGA spectra of the BQ-Tg and BQ-To PDs. (d) XPS survey spectra of the BQ-Tg and BQ-To PDs. (e,f) XPS fitting curves of the (e) C1s for the BQ-Tg and (f) C1s for the BQ-To PDs.

temperatures; hence, the TGA curves effectively indicate the good thermal stability of synthesized PDs. To rationalize the higher thermal stability of BQ-Tg PDs compared with BQ-To PDs, we measured the TGA profiles of the corresponding diamine monomers (Fig. S10). As shown, Tg-2NH_2 exhibits a delayed onset of weight loss and a more gradual decomposition than To-2NH_2, confirming that the Tg-based precursor is intrinsically more thermally robust. This enhanced stability can be attributed to the higher nitrogen content and the rigid V-shaped Tröger's base scaffold, which increases structural rigidity and strengthens intermolecular interactions, thereby suppressing thermal cleavage [34,45,46]. Consequently, the superior thermal stability of BQ-Tg PDs relative to BQ-To PDs is primarily inherited from the greater intrinsic thermal resistance of Tg-2NH_2, and further reinforced by the more rigid, N-rich framework formed in the Tg-derived polymer dots. XPS analysis was applied to validate the elemental composition of the synthesized PDs. Fig. 1d illustrates that no extraneous components were identified, signifying the lack of obvious contaminants in the conjugated polymers throughout production. The spectra additionally indicated the existence of two different peaks associated with C 1 s and N 1 s orbitals, displaying two distinct peaks at 284 and 398 eV for the BQ-Tg PDs, and at 283 and 398 eV for the BQ-To PDs. Furthermore, a peak at 531 eV is detected, indicating the presence of adsorbed water and oxygen.

We fitted the XPS patterns for the C 1 s, N 1 s, and O 1 s orbitals (Figs. 1e, 1f, S11, and Table S2) to have a better grasp of the types of element species shown in the PDs. The C 1 s orbital for the BQ-Tg PDs has four separate peaks: 283.08 eV for C═C, 283.65 eV for C—C, 284.49 eV for C—N, and 285.65 eV for C═O (Fig. 1e and Table S2). Whereas the BQ-To PDs demonstrated similar peaks at energy values of 282.96, 283.71, 284.51, and 285.67 eV (Fig. 1f and Table S2). The N 1 s orbital of the BQ-Tg PDs displayed two distinct peaks at 397.72 and 398.55 eV, corresponding to the N-bridge and N-amino groups, respectively (Fig. S11a and Table S2). Furthermore, the BQ-Tg PDs exhibited two distinct peaks in the O 1 s spectrum: C═O and H_2O at energy values of 530.62 and 531.72 eV, respectively (Fig. S11b and Table S2). Conversely, the BQ-To PDs demonstrated equivalent peaks at energy values of 530.58 and 531.63 eV, respectively (Fig. S11c and Table S2). Table S3 summarizes the XPS deconvolution ratios of the surface bonding environments for BQ-Tg and BQ-To polymer dots, highlighting clear differences in their carbonyl- and nitrogen-related species, which are directly relevant to their electrochemical behavior. In the C 1 s region, both samples show similar aromatic C═C contents (~41%), indicating comparable conjugated backbones, while the relative fractions of C—C, C—N, and C═O differ. Notably, BQ-Tg PDs exhibit a higher C—N contribution (29.96%) than BQ-To PDs (21.43%), whereas BQ-To PDs show a higher apparent C═O component in C 1 s (10.76%) compared with BQ-Tg PDs (5.64%). In the N 1 s region, BQ-Tg PDs contain two nitrogen environments—nearly equal N-bridge (49.70%) and N-amino (50.30%)—consistent with incorporation of the Tröger's-base bridging nitrogen together with amine-type nitrogen, while BQ-To PDs display only N-amino (100%) with no N-bridge contribution. The O 1 s fitting shows comparable partitioning between C═O and adsorbed H_2O for both samples, suggesting similar oxygen-containing surface environments overall. Based on these data, BQ-Tg PDs are expected to deliver higher capacitance than BQ-To PDs because the higher C—N content and the presence of N-bridge species provide a more nitrogen-rich, electronically coupled framework that can enhance electrode polarity and facilitate faster interfacial charge transfer and ion transport, thereby improving the effective utilization of redox-active sites during cycling. In contrast, although BQ-To exhibits a higher C═O fraction, its lack of an N-bridge and lower C—N contribution can lead to less efficient charge transport and higher polarization, thereby reducing active-site utilization and limiting the attainable capacitance. Overall, the XPS-derived bonding distributions suggest that BQ-Tg PDs should deliver higher supercapacitor capacitance, as they couple accessible quinone redox sites with a nitrogen-bridged, electronically favorable network that promotes fast and reversible charge storage. Tables S4 and S5 compare the theoretical and XPS-derived experimental atomic ratios (At.%, excluding H) of BQ-Tg and BQ-To polymer dots, showing excellent agreement that supports the proposed compositions. For BQ-Tg PDs, the theoretical ratios (C/N/O = 69.71/14.14/16.15 At.%) closely match the experimental values (69.99/14.14/15.87 At.%), indicating that the synthesized material retains the expected nitrogen-rich framework and

oxygen functionalities. Similarly, for BQ-To PDs, the theoretical composition (62.92/11.29/25.79 At.%) is consistent with the experimental ratio (62.51/11.62/25.87 At.%), confirming its higher oxygen content relative to BQ-Tg. Overall, the close theoretical–experimental consistency validates successful incorporation of the designed heteroatom contents in both polymer dots and confirms that the observed differences between BQ-Tg (higher N) and BQ-To (higher O) arise from their intended structural design rather than impurities. XRD study of BQ-Tg and BQ-The PDs exhibited no detectable diffraction peaks, emphasizing their amorphous characteristics, as previously documented for other PDs (Fig. S12) [10,47]. The lack of lattice borders in PDs shows that they are amorphous [47]. The abundance of hydrophilic chemical compounds in the PDs serves as a surfactant to improve conductivity and optimize the porous architectures of PDs [48].

3.2. Morphology studies

Transmission electron microscopy (TEM), scanning electron microscopy (SEM), and energy dispersive X-ray spectroscopy (EDS) were used to analyze the morphology and elemental composition of synthesized PDs (Figs. 2a-h, S13, and S14). The BQ-Tg PDs (Figs. 2a–d) exhibited a uniform distribution of well-dispersed spherical polymer dots with smooth surfaces. The average particle size was measured to be approximately 45–60 nm, with a narrow size distribution, confirming the successful formation of nanoscale structures through the one-step reaction. At higher magnifications, the spherical morphology and well-defined boundaries of the BQ-Tg PDs were clearly visible, indicating high structural uniformity. In contrast, the BQ-To PDs (Figs. 2e–h) displayed a less uniform morphology, with particles exhibiting interconnected or aggregated structures. The average particle size of the BQ-To dots was slightly larger, ranging from 55 to 80 nm, and the tendency for aggregation was more pronounced compared to the BQ-Tg PDs. These observations suggest that the rigid Tröger's base framework in the BQ-Tg PDs helps restrict excessive growth and aggregation, yielding smaller and more monodisperse polymer dots, whereas the flexible toluene diamine leads to relatively larger and less uniform nanostructures. Overall, TEM analysis confirms the nanoscale formation of both BQ-Tg and BQ-To PDs, with the BQ-Tg system showing superior size control and particle uniformity. The surface morphology of the synthesized polymer dots was also examined using SEM combined with EDS. For the BQ-Tg PDs (Fig. S13a–c), SEM images revealed well-dispersed spherical nanoparticles with relatively smooth surfaces and moderate aggregation at higher magnifications. The EDS elemental mapping (Fig. S13d–f) confirmed the uniform distribution of carbon (C), nitrogen (N), and oxygen (O) throughout the polymer framework, consistent with the expected composition from the benzoquinone and Tröger's base diamine precursors. In the case of the BQ-To PDs (Fig. S14a–c), SEM images showed nanosized particles with a tendency toward chain-like aggregation, suggesting less steric hindrance compared to the rigid Tröger's base structure. The EDS maps (Fig. S14d–f) again demonstrated the homogeneous presence of C, N, and O, verifying the successful incorporation of benzoquinone and toluene diamine units into the polymer network. Collectively, the SEM and EDS analyses confirm the nanoscale morphology of both BQ-Tg and BQ-To PDs, validating their elemental compositions and supporting the efficient one-step synthesis route. Dynamic light scattering (DLS) measurements were carried out to further evaluate the particle size distribution of the synthesized polymer dots. As shown in Fig. S15a, the BQ-Tg PDs exhibited a narrow size distribution centered around ~58 nm, indicating the formation of relatively uniform nanoscale particles with good dispersibility. The sharpness of the peak suggests limited aggregation, which is consistent with the spherical morphology observed in TEM and SEM analyses. In contrast, the BQ-To PDs (Fig. S15b) displayed a broader size distribution, with an average particle size of ~72 nm and a slight tailing toward larger diameters. This wider distribution reflects the greater tendency of BQ-To particles to form interconnected or aggregated structures, as also observed in electron microscopy. Overall, the DLS data confirm that both polymers exist in the nanoscale regime, with BQ-Tg PDs demonstrating superior monodispersity and size control compared to BQ-To PDs, owing to the structural rigidity imparted by the Tröger's base linker.

3.3. Electrochemical properties

The BQ-based PDs were systematically evaluated for their electrochemical properties using cyclic voltammetry (CV) and galvanostatic charging and discharging (GCD) tests within a three-electrode layout (Fig. 3a-d) [49]. Assessments were performed in the potential window from +0.00 to −1.00 V in a 3 M KOH aqueous electrolyte, utilizing a glassy carbon electrode for the working electrode, a platinum electrode as the counter electrode, and an Hg/HgO electrode as the reference electrode. Figs. 3a and 3b indicate that the CV profiles of both PDs, assessed at scans of 5 to 200 mV s^{-1}, have a similar modestly skewed rectangular shape, due to the combined impact created by EDLC and pseudocapacitance. The oxidation and reduction peak potentials for BQ-Tg PDs were recorded at −0.44 V and − 0.61 V, respectively, during a

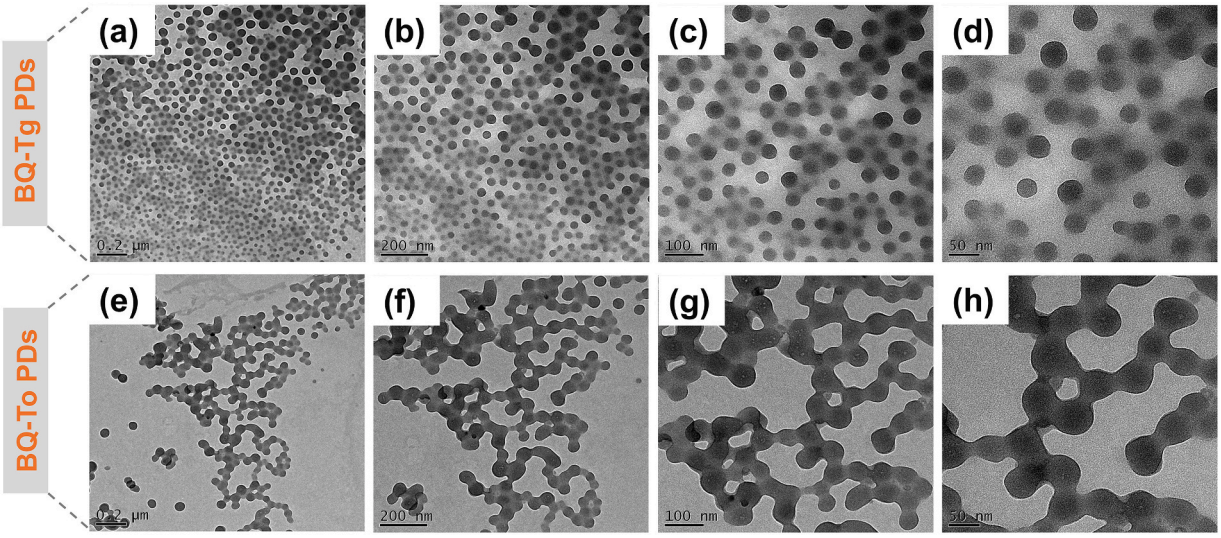

Fig. 2. TEM images of (a-d) BQ-Tg and (e-h) BQ-To PDs.

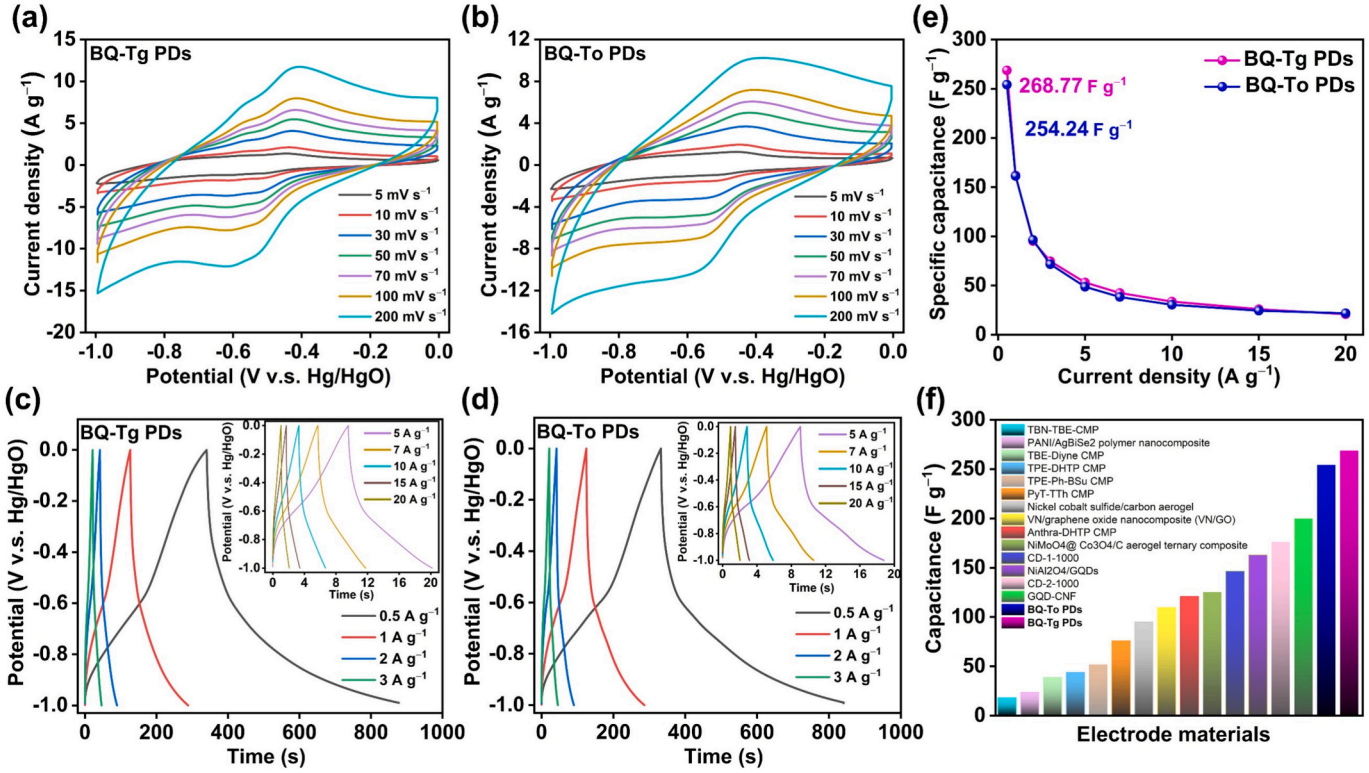

Fig. 3. (a,b) CV profiles and (c,d) GCD profiles of (a,c) the BQ-Tg and (b,d) BQ-To PDs, tested at various scans. (e) Specific capacitances of the BQ-Tg and BQ-To PDs, tested at various current densities. (f) Specific capacitances of the BQ-Tg and BQ-To PDs compared to earlier documented polymers.

scan at 5 mV s^{-1}. Conversely, the BQ-To PDs demonstrated values of −0.45 V and − 0.51 V (Figs. 3a and 3b). Once the scan rate increased from 5 to 200 mV s^{-1}, the oxidation peak potential exhibited a positive shift, while the reduction peak potential demonstrated a negative shift. The elevation in scan rate resulted in the input impedance of the BQ-Tg and BQ-To PDs-coated electrodes widening the spacing between the oxidation and reduction peaks (Figs. 3a and 3b) [50]. Regardless of this, the CV curves of both PDs preserved their overall structure upon increasing the scan rate potential from 5 to 200 mV s^{-1}, indicating their accelerated electrochemical kinetics and superior rate performance [51]. The minimal range between the oxidation and reduction peaks signifies effective electron flow between Tg and BQ units in BQ-Tg PDs, as well as between To and BQ units in BQ-To PDs. Collectively, these observations confirmed the quasi-reversible nature of the redox processes, ascribed to the existence of redox-active benzoquinone moieties and heteroatoms, including oxygen and nitrogen. CV figures indicate that the variations in anodic and cathodic peak potentials with elevated scan rates are due to kinetic barriers in ion transport and charge transfer at the electrode/electrolyte interface [52]. At lower scan rates, ions can effectively diffuse into the electrode material, facilitating thermodynamically aligned redox peaks. Conversely, as the scan rate grows, the reduced time for ion diffusion generates concentration polarization, resulting in the observed peak shifting. This phenomenon aligns with research indicating that diffusion-controlled processes occur at increased scan rates, causing peak potential shifts [53,54]. Moreover, elevated scan rates result in increased overpotentials due to elevated resistive losses in both the electrolyte and electrode materials, further causing peak shifts [54]. These findings are consistent with recent research indicating that higher scan rates lead to increased charge transfer resistance and diminished capacitive performance [55]. This dependence on scan rate demonstrates the interplay between capacitive surface processes and diffusion-limited faradaic contributions, which is essential for optimizing supercapacitor performance [56].

Figs. 3c and 3d illustrate that the GCD curves of BQ-Tg and BQ-To PDs, evaluated over current densities of 0.5 to 20 A g^{-1}, exhibit approximately symmetric triangle-shaped forms, hence affirming the pseudocapacitive characteristics of these electrodes [57,58]. Elevated current densities result in an augmented concentration of charge carriers, which therefore increases the electrolyte's impedance and diminishes the effective flow rate [59]. The BQ-Tg PD shows a slightly longer discharge time than BQ-To PD, indicating a higher specific capacitance. This improvement is consistent with its smaller polymer-dot size (DLS mean diameter ~ 58 nm for BQ-Tg vs ~72 nm for BQ-To), which increases electrolyte-accessible surface area and shortens ion-diffusion pathways, enhancing rate kinetics and active-site utilization. In addition, XPS confirms that BQ-Tg is more N-rich (higher N atomic percentage and a larger C—N contribution) and uniquely contains N-bridge species, which can improve electrode polarity and facilitate interfacial charge transfer, thereby strengthening pseudocapacitive contributions. Collectively, the smaller dot size and higher nitrogen content/bonding density in BQ-Tg PD provide a more favorable structure for rapid and reversible charge storage, explaining its higher capacitance relative to BQ-To PDs [60]. The specific capacitances of the BQ-Tg and BQ-To PDs were calculated using Eq. (S2), yielding values of 268.77 F g^{-1} and 254.24 F g^{-1} at a current density of 0.5 A g^{-1}, respectively (Fig. 3e). The BQ-Tg PDs demonstrated a higher specific capacitance, which is in accordance with the results gathered from both CV and GCD measurements. Notably, both PDs exhibited elevated capacitance values, attributable to the existence of redox-active moiety (BQ), their abundant heteroatom content as well as their nanoscale and uniform particle size, which collectively enhance ion transport and charge storage efficiency [10,61]. Fig. 3f and Table S6 indicate that the BQ-Tg and BQ-To PDs possess specific capacitances that surpass those of comparable polymers, such as TBN-TBE-CMP (18.45 F g^{-1} at 0.5 A g^{-1}) [62], PANI/AgBiSe2 polymer nanocomposite (24 F g^{-1} at 1 mA g^{-1}) [63], TBE-Diyne CMP (39 F g^{-1} at 0.5 A g^{-1}) [64], TPE-DHTP CMP (44 F g^{-1} at 0.5 A g^{-1}) [65], TPE-Ph-BSu CMP (52 F g^{-1} at 0.5 A g^{-1}) [66], PyT-TTh CMPs (76 F g^{-1} at 0.5 A g^{-1}) [67], Nickel cobalt sulfide/carbon

aerogel derived from waste watermelon rind (95 F g^{-1} at 1 A g^{-1}) [68], VN/graphene oxide nanocomposite (VN/GO) (109.7 F g^{-1} at 1 A g^{-1}) [69], Anthra-DHTP CMP (121 F g^{-1} at 0.5 A g^{-1}) [65], NiMoO4@Co3O4/Carbon aerogel ternary composite (125.4 F g^{-1} at 0.5 A g^{-1}) [70], CD-1-1000 (146.5 F g^{-1} at 1 A g^{-1}) [71], NiAl2O4/GQDs (163 F g^{-1} at 1 A g^{-1}) [72], CD-2-1000 (176.3 F g^{-1} at 1 A g^{-1}) [71], and GQD-CNF (200 F g^{-1} at 1 A g^{-1}) [73]. Compared with inorganic Faradaic materials, our BQ-Tg and BQ-To PDs provide superior advantages due to their facile synthesis, lightweight nature, ease of processing, uniform particle size, and existence of redox-active unit (BQ) combined with high heteroatom content [74,75]. These characteristics collectively enhance ion diffusion, electrical conductivity, and overall capacitive performance. The small IR drop at the beginning of the discharge curve is mainly due to the device's equivalent series resistance (ESR) [17,76], i.e., the IR (ohmic) drop caused by the resistance of the electrolyte between the working and reference electrodes [77]. On the other hand, this effect does not significantly impact the conductivity of the electrodes or their ability to impede charge. This effect is commonly observed in three-electrode measurements: when a significant current passes through the solution, a voltage drop develops across the solution resistance, and it becomes more pronounced when the working and reference electrodes are relatively far apart. Importantly, this initial IR drop is a measurement-related resistance loss and does not indicate a substantial change in the electrode conductivity or charge-transfer barrier [77].

Figs. S16a–c compare the cyclic voltammograms of the building blocks BQ, Tg-2NH_2, and To-2NH_2 measured at 5 and 10 mV s^{-1} (vs. Hg/HgO). In all cases, increasing the scan rate from 5 to 10 mV s^{-1} increases the current response while largely preserving the curve shape, indicating stable electrochemical behavior over this rate range. Notably, BQ shows a more pronounced faradaic contribution (broader redox-related features) consistent with its intrinsically redox-active quinone unit, whereas Tg-2NH_2 and To-2NH_2 monomers displayed almost rectangle-shaped cyclic voltammetry patterns, indicative of their electric double-layer activity. Overall, these CVs highlight that the strong redox activity originates from the BQ moiety, which later underpins the pseudocapacitive charge-storage mechanism when incorporated into the polymer-dot framework. Conversely, the BQ units embedded in the BQ-Tg and BQ-To polymer dots act as the dominant redox-active sites and undergo a reversible two-electron conversion during charge/discharge (Figs. 4a and S17a). Upon discharge, the carbonyl-containing BQ moiety is reduced stepwise (BQ → BQ•$^-$ → BQ^{2-}), accompanied by charge compensation through the electrolyte (K^+ association), yielding a hydroquinone (quinone-dianion)–type reduced state; the reverse oxidation restores the original quinone form during charging [78]. This mechanism is directly supported by ex-situ FTIR collected from electrodes stopped at selected states (pristine/oxidized, discharged/reduced, and re-oxidized) (Figs. S18, 4b and 4c), which shows a pronounced and reversible change in the characteristic vibrational bands: the C═O stretching region (~1650–1680 cm^{-1}) decreases upon discharge (reduction of quinone carbonyls) (Fig. 4b), while a C–O-related band (~1200–1250 cm^{-1}) becomes stronger in the reduced state (Fig. 4c), consistent with formation of reduced quinone species; significantly, both features essentially recover after recharging, confirming a highly reversible quinone redox process and explaining the pseudocapacitive contribution observed in the CV profiles.

In BQ-Tg PDs, the charge storage is governed by the reversible quinone redox chemistry of the benzoquinone units covalently embedded in the polymer-dot framework (Fig. 4d). During discharge (reduction), the quinone carbonyls accept two electrons (often proceeding through a semiquinone radical intermediate) to form a reduced quinone state that can be described as a dianion/hydroquinone-like species (BQ-Tg^{2-}), with charge compensation provided by the alkaline electrolyte (association of K^+). Upon charge (oxidation), the reduced quinone species is converted back to the original quinone form, regenerating the C═O groups and enabling highly reversible faradaic cycling. The redox reaction of BQ occurred as a single pair of stacking up, as evidenced by the appearance of redox peaks at −0.44 and − 0.61 V in the CV curve (Fig. 3a). This mechanism is directly supported by the ex-situ FTIR spectra collected from electrodes at different states (oxidized/pristine, discharged/reduced, and re-oxidized) (Figs. S19, 4e, and 4f). In the C═O stretching region (~1650–1680 cm^{-1}), the intensity decreases markedly after discharge, consistent with consumption/reduction of quinone carbonyls (Fig. 4e). Simultaneously, a band in the C—O region

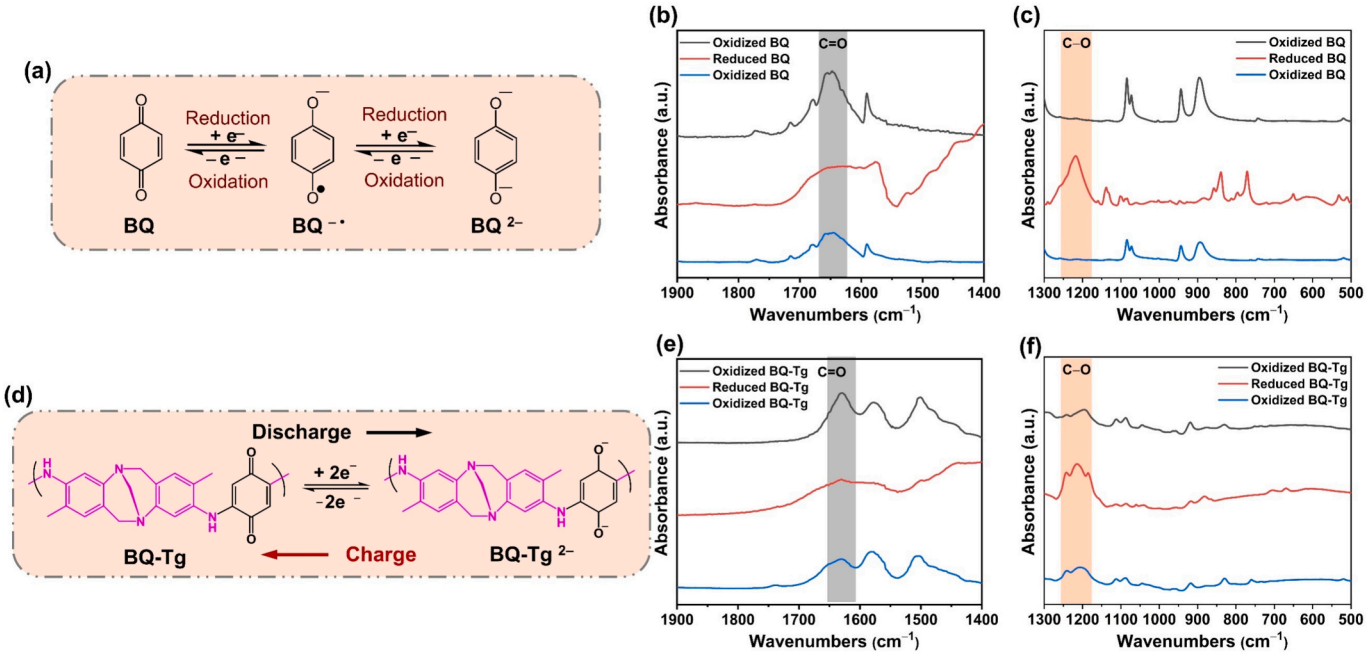

Fig. 4. (a) Proposed redox mechanism of the BQ. (b–c) Ex-situ FT-IR spectra of BQ-based electrode at oxidized/reduced/re-oxidized states: (b) C═O region 1900–14,000 cm^{-1} and (c) C—O region 1300–500 cm^{-1}. (d) Proposed redox mechanism of the BQ-Tg PDs. (e–f) Ex-situ FT-IR spectra of BQ-Tg PD-based electrode at oxidized/reduced/re-oxidized states: (e) C═O region 1900–1400 cm^{-1} and (f) C—O region 1300–500 cm^{-1}.

(~1200–1250 cm^{-1}) becomes stronger in the reduced state, indicating formation of reduced quinone (C–O^{-}/C–O) functionalities (Fig. 4f). Significantly, after recharging the electrode, the C═O band essentially recovers, and the C—O feature diminishes toward the initial state, confirming that these vibrational changes are reversible and arise from the quinone/reduced-quinone redox conversion within the BQ-Tg polymer dots. Similarly, the redox-dependent behavior of the BQ-To PDs is illustrated in Figs. S17a and S17b. The charge-storage mechanism is dominated by the reversible two-electron redox conversion of the BQ moieties covalently incorporated into the polymer-dot framework. During discharge (reduction), the quinone unit accepts $2e^{-}$ (often via a semiquinone intermediate) to form the reduced state that can be represented as a dianion/hydroquinone-like species (BQ-To^{2-}), where the original carbonyl groups are converted into alkoxide-type C—O functionalities; charge neutrality is maintained by the alkaline electrolyte through association with K^{+} (Fig. S17b). Upon charge (oxidation), the reduced quinone species is reversibly oxidized back to the original quinone, regenerating the C═O groups, which enables stable pseudocapacitive cycling. The redox peaks identified in the CV curve at −0.45 and − 0.51 V validate a singular pair of redox events associated with the BQ units (Fig. S17b).

To further investigate the ionic/electronic transport and interfacial kinetics of the BQ-Tg and BQ-To PDs, electrochemical impedance spectroscopy (EIS) measurements were conducted. Impedance spectra were recorded over a frequency range of 0.01 Hz to 100 kHz by plotting the real component (Z′) on the X-axis and the negative imaginary component (−Z″) on the Y-axis. Fig. 5a shows the Nyquist plots of both BQ-Tg and BQ-To PDs-based electrodes. In the high-frequency region, both plots exhibit small semicircles, indicating low charge-transfer resistance and efficient ion transport within the electrolyte. In the low-frequency region, the curves approach a near-vertical line, characteristic of dominant capacitive behavior [79]. This low-frequency response can also include a diffusion (Warburg) contribution arising from ion transport within the electrode/electrolyte interface; as diffusion limitations decrease and capacitive storage dominates, the line becomes more vertical [80]. The intrinsic ohmic resistance (*Rs*) was obtained from the high-frequency intercept on the Z′ axis of the Nyquist plot, representing the series resistance of the cell (including electrolyte, current collector, and contact/electrode resistances), and thus reflecting the overall ohmic loss in the PD-coated electrodes [81,82]. The *Rs* values for BQ-Tg and BQ-To PDs were 3.91 and 5.02 Ω, respectively (Fig. 5a). The lower *Rs* of BQ-Tg indicates reduced internal ohmic resistance, enabling more efficient electron/ion transport and a smaller IR drop, which contributes to improved rate performance. Fig. 5b shows the equivalent circuit used to fit the Nyquist plots. Here, *Rs* is the ohmic (series) resistance, *R*ct is the charge-transfer resistance, CPE1 represents the double-layer capacitance at the electrode–electrolyte interface, and W denotes the Warburg diffusion impedance. The fitted values (Table S7) reveal clear kinetic differences between the two electrodes. BQ-Tg PDs exhibit a lower *Rs* of 3.91 Ω (3.2% error) than BQ-To PDs (5.02 Ω, 2.9% error), indicating reduced internal/series resistance and more efficient transport charge. More importantly, the *R*ct of BQ-Tg PDs is dramatically smaller (75.81 Ω, 4.87% error) than that of BQ-To PDs (500 Ω, 5.47% error), confirming much faster interfacial charge-transfer kinetics for BQ-Tg, consistent with its superior rate capability and higher capacitance [83]. The CPE1 values are comparable (0.80 vs 0.71), suggesting similar capacitive behavior. Overall, the fitting indicates that the performance advantage of BQ-Tg PDs primarily originates from lower *Rs* and, especially, much lower *R*ct, enabling faster and more reversible charge storage. Fig. 5c provides the Bode phase angle diagrams for BQ-Tg and BQ-To PDs. The phase angle of −45° signifies the relaxation time constant (τ_0), reflecting how quickly the electrode responds to charge/discharge. BQ-Tg PDs exhibits a shorter relaxation time (8.3×10^{-5} s) than BQ-To PDs (1.0×10^{-4} s), signifying accelerated ion transport and enhanced charge-transfer kinetics. This outcome validates the enhanced electrochemical performance of both PDs, particularly the BQ-Tg PDs. Fig. 5d reveals the cycling stability of BQ-Tg and BQ-To PDs across 10,000 charge-discharge cycles. The BQ-Tg PDs preserve 79.3% of their initial capacitance, whereas the BQ-To PDs maintain 69.64%. This signifies the enduring electrochemical stability and adaptability of the synthesized PDs. The improved durability of BQ-Tg is primarily attributed to its more robust and nitrogen-bridged framework, as well as its smaller dot size, which together stabilize the redox sites and reduce polarization during prolonged cycling. XPS confirms that BQ-Tg contains a higher C—N content and characteristic N-bridge species, which strengthen the covalent framework and facilitate more efficient interfacial charge transfer, thereby reducing side reactions and maintaining reversible quinone redox activity over

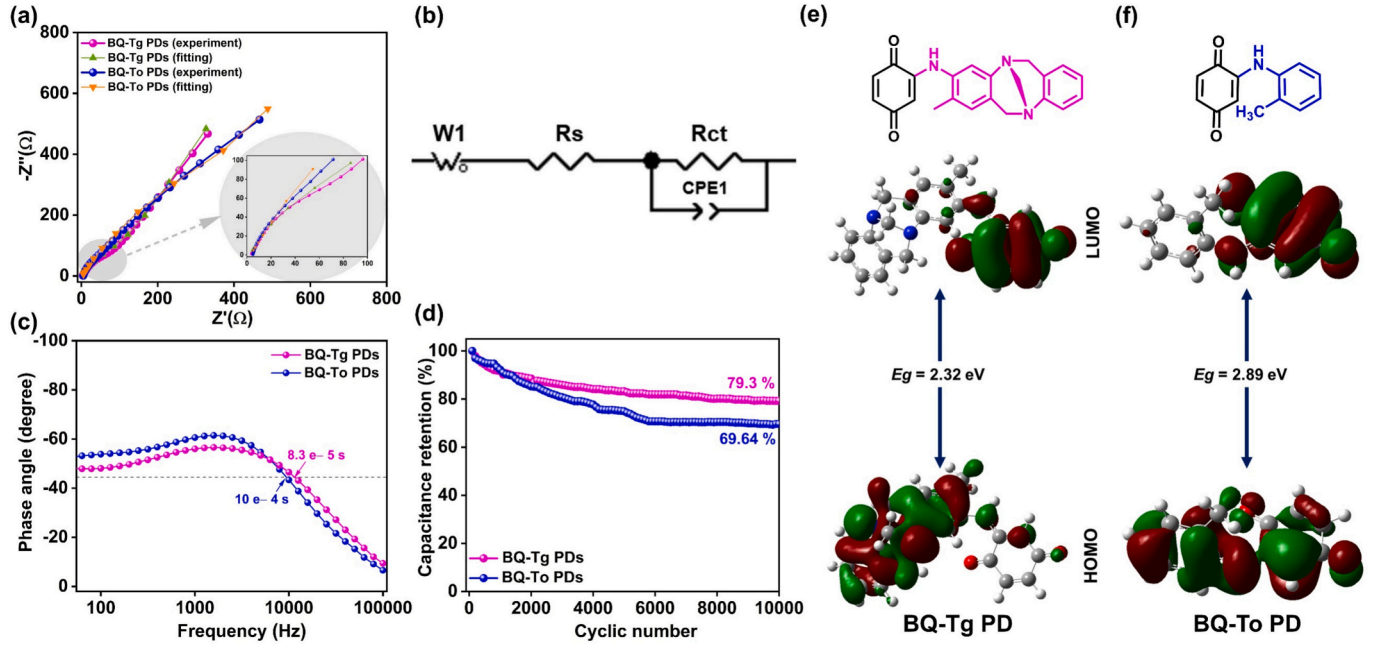

Fig. 5. (a) EIS and the fitted Nyquist plot that corresponded, (b) equivalent circuit, (c) Bode plots, and (d) extending cycling efficiency of the BQ-Tg and BQ-To PDs. The stability is recorded at a current density of 10 A g^{-1}. (e,f) The HOMO-LUMO distributions and band-gap (Δ*E*) values of (e) BQ-Tg and (f) BQ-To PDs.

repeated cycles [46]. In addition, DLS shows a smaller mean diameter for BQ-Tg (~58 nm vs ~72 nm for BQ-To), which shortens ion-diffusion pathways and mitigates local concentration polarization, further suppressing performance decay at extended cycling. Importantly, the TGA results further support this interpretation: BQ-Tg PDs display slightly higher thermal stability ($T_{d10}\%$ = 387.04 °C) than BQ-To PDs ($T_{d10}\%$ = 380.95 °C), consistent with a more stable framework that is less prone to structural degradation under repeated electrochemical operation [45]. Consistently, EIS fitting indicates lower internal resistance and a much smaller *Rct* for BQ-Tg, supporting more stable kinetics during cycling. We employed Gaussian 05 software to compare the electronic structures of the Tg- and To-derived building blocks and to rationalize their distinct electrochemical behaviors using density functional theory (DFT) calculations at the B3LYP/6-31G* level. Fig. 5e and f illustrate the highest occupied molecular orbitals (HOMOs) and the lowest unoccupied molecular orbitals (LUMOs) of these PDs. The BQ-Tg PDs (Fig. 5e) display a reduced HOMO-LUMO energy gap relative to the BQ-To PDs (Fig. 5f). A reduced band gap indicates stronger electronic delocalization and easier charge excitation/transport, which is beneficial for electron transfer during redox charging/discharging [17]. The orbital plots further suggest that the frontier orbitals are more effectively delocalized over the conjugated framework in the Tg-based structure, whereas the To-based structure shows comparatively less favorable delocalization, consistent with its larger band gap. Overall, the DFT results suggest that the Tg-derived framework should exhibit higher intrinsic electronic conductivity and faster charge-transfer kinetics, which supports the experimentally observed lower impedance and improved capacitive performance of the BQ-Tg polymer dots compared to BQ-To [17,84].

We used the following power law equation (eq. (1)) to investigate the relationship between electrical current (i) and scan rate (v) in order to further understand the capacitive contribution of BQ-Tg and BQ-To PDs [85].

$$i = av^b \tag{1}$$

In this work, both constants a and b were determined, with the b value derived from the slope of a plot of log(i) versus log(v), where i signifies the current and v represents the scan rate. A b value of 1 indicates a capacitive interpretation, while a value of 0.5 signifies a diffusion-controlled process. A capacitive-controlled process generates electric double-layer capacitance through the accumulation and physisorption of ions from the electrolyte on the electrode surface. In contrast, a diffusion-controlled process produces pseudocapacitance by facilitating the diffusion of electrolyte ions through the material to engage in Faradaic reactions. Figs. 6a and 6b demonstrate that the estimated b values for the BQ-Tg PDs are 0.64 for the cathodic peak and 0.58 for the anodic peak. In contrast, the BQ-To PDs exhibits b values of 0.65 for the cathodic peak and 0.57 for the anodic peak (Fig. 6b). The findings indicate that these two PDs utilize capacitive and diffusion-controlled techniques for preserving energy [86].

The proportion of the contribution can be determined utilizing the following (Eq. (2)) [85].

$$i(V) = k_1 v + k_2 v^{1/2} \tag{2}$$

In this sense, *i(V)* denotes the current response at a particular potential *V*, whereas $k_1 v$ and $k_2 v^{1/2}$ pertain to the effects of capacitive electric charge retention and diffusion-controlled mechanisms, respectively. At a scanning rate of 5 mV s^{-1}, the capacitive impact was measured at 12% for the BQ-Tg PDs and 10% for the BQ-To PDs (Figs. 6c and 6d). BQ-Tg PDs demonstrated a higher capacitive contribution, indicating that both heteroatoms and homogeneous pore size are essential in improving surface-controlled charge storage. Figs. 6e and 6f illustrate the progression in capacitive contribution as the scan rate increases from 5 to 200 mV s^{-1}. In synthesized PDs, the capacitive portion exhibited a substantial rise with scan rate, attaining 47% in BQ-Tg PDs and 40% in BQ-To PDs. The reduction in the diffusive component and the augmentation of the capacitive component result from the ions' interaction duration with the electrode material at both low and high scan rates. The results indicate that at elevated scan rates, capacitive

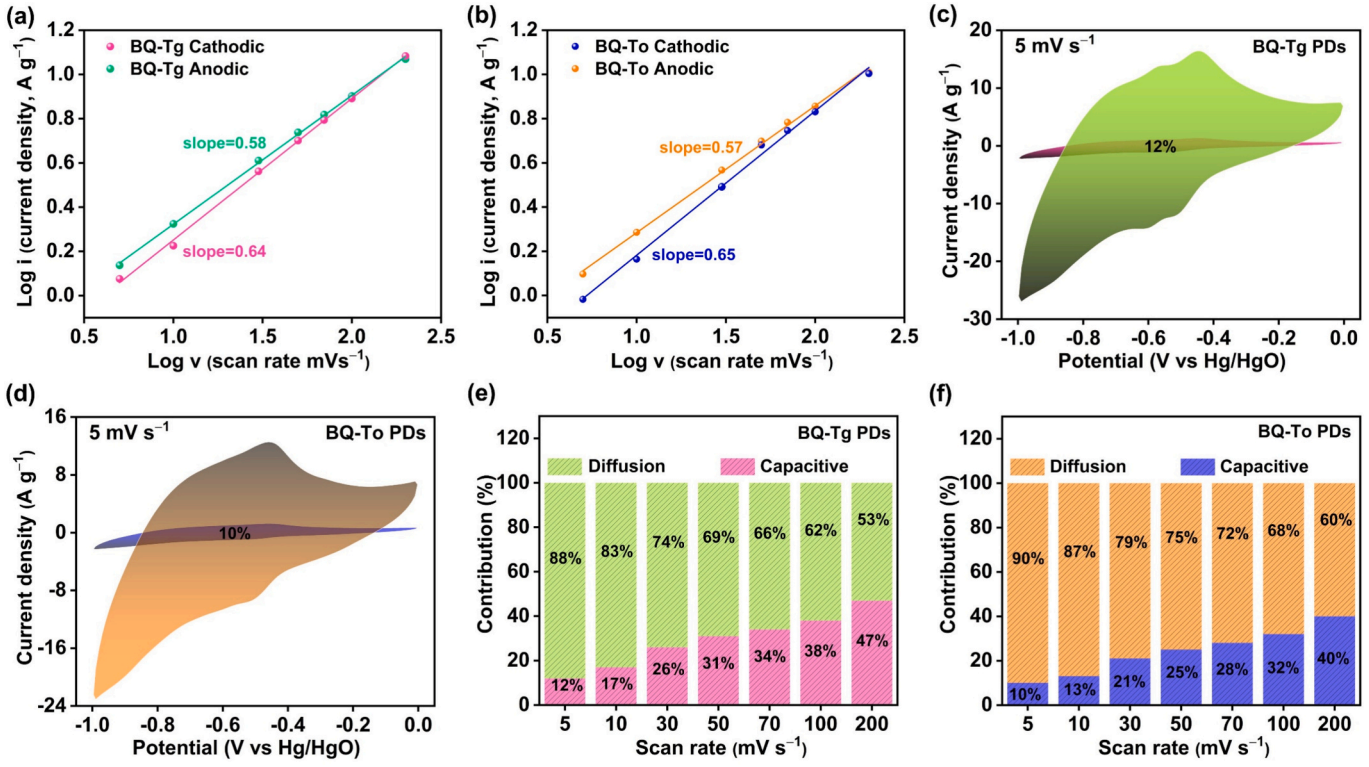

Fig. 6. (a,b) Graphs of log(i) vs log(*v*) and (c, d) capacitive and diffusion contributions, recorded at 5 mV s^{-1} of (a,c) BQ-Tg and (b,d) BQ-To PDs. (e,f) Capacitive and diffusion-controlled storage for charges of (e) BQ-Tg and (f) BQ-To PDs at different scans.

processes prevail because of the minimal time available for ion diffusion. The observations suggest that a high ratio of heteroatoms and uniform distribution of well-dispersed spherical polymer dots, particularly in BQ-Tg PDs, significantly improve electrochemical efficiency by promoting the swift transport of ions and enhancing surface redox activity.

Importantly, the nanoparticle dimensions of active materials in supercapacitor electrodes strongly influence energy-storage behavior by governing ion accessibility, charge transport, and surface reactivity [87]. In general, smaller polymer dots provide a higher surface area per unit mass, which increases electrolyte contact with electroactive sites and promotes both electric double-layer formation and pseudocapacitive redox processes, thereby improving specific capacitance and energy density [87]. Moreover, smaller particle size shortens ion-diffusion pathways and reduces diffusion resistance, enabling faster ion transport and enhanced rate capability in CV and GCD measurements [88]. Consistent with prior studies, electrodes with smaller and more uniform particles typically show better electrolyte penetration, reduced polarization, and lower internal resistance, leading to more stable capacitance at high scan rates/current densities [89,90]. By contrast, larger particles can hinder ion diffusion and decrease active-site utilization, reducing overall charge-storage efficiency [88]. In our system, the polymer dots form nanoscale, well-dispersed particles (confirmed by SEM/TEM and DLS), which increase the electrolyte-accessible surface area, shorten ion-diffusion lengths, and facilitate faster electron transport through the electrode network, thereby improving rate capability and reversibility of the quinone redox reaction. Moreover, the size difference between BQ-Tg and BQ-To (DLS mean diameter: ~58 nm for BQ-Tg vs. ~72 nm for BQ-To) supports the notion that the smaller dots provide higher active-site utilization and reduced polarization, which is consistent with their comparatively better capacitive response.

Overall, the higher capacitance of BQ-Tg PDs compared with BQ-To PDs arises from a more favorable combination of morphology, composition, and charge-transfer kinetics. DLS confirms that BQ-Tg forms smaller dots (~58 nm) than BQ-To (~72 nm), which increases electrolyte-accessible surface area, shortens ion-diffusion pathways, and improves active-site utilization at practical rates. XPS further shows that BQ-Tg is more N-rich and uniquely contains N-bridge species with a higher C—N contribution, which enhances surface polarity and strengthens electronic coupling within the framework, promoting more efficient interfacial charge transfer. Consistently, EIS fitting reveals markedly faster kinetics for BQ-Tg, with lower *Rs* (3.91 Ω) and especially much smaller *Rct* (75.81 Ω) than BQ-To (*Rs* 5.02 Ω; *Rct* 500 Ω), indicating reduced polarization and improved reversibility of the quinone redox process. In addition, BQ-Tg shows slightly higher thermal robustness (T_{d10}% 387.04 °C vs 380.95 °C), supporting a more stable framework during repeated operation, while DFT calculations suggest a more favorable electronic structure for the Tg-based unit (smaller band gap), facilitating electron transport. Together, these factors enable faster ion/electron transport and more effective, reversible utilization of redox-active sites, leading to the higher capacitance of BQ-Tg PDs.

To enable the practical application of the synthesized BQ-Tg PDs in a device, its electrochemical performance in a symmetric supercapacitor (SSC) was assessed, with our polymer serving as both the cathode and anode in the SSC. A 3 M solution of KOH in water functioned as the electrolyte in the apparatus, including two similar BQ-Tg PDs-based electrodes set on carbon sheets and isolated by a filter paper barrier (Fig. 7a). CV measurements were conducted within a potential range of 0.0 to +1.0 V at scan rates between 5 and 500 mV s^{-1}. The resultant CV curves displayed semi-rectangular patterns with quasi-reversible redox characteristics that maintained stability over the scan range, signifying quick electrolyte diffusion and effective charge storage behavior (Fig. 7b). Fig. 7c depicts the GCD plots for current densities between 0.7 A g^{-1} to 11.1 A g^{-1} of the BQ-Tg PDs-based supercapacitor device. The specific capacitance of the BQ-Tg PDs tethered supercapacitor can be estimated from the mass of the individual electrodes at different current densities (Fig. 7d). The specific capacitance was calculated according to

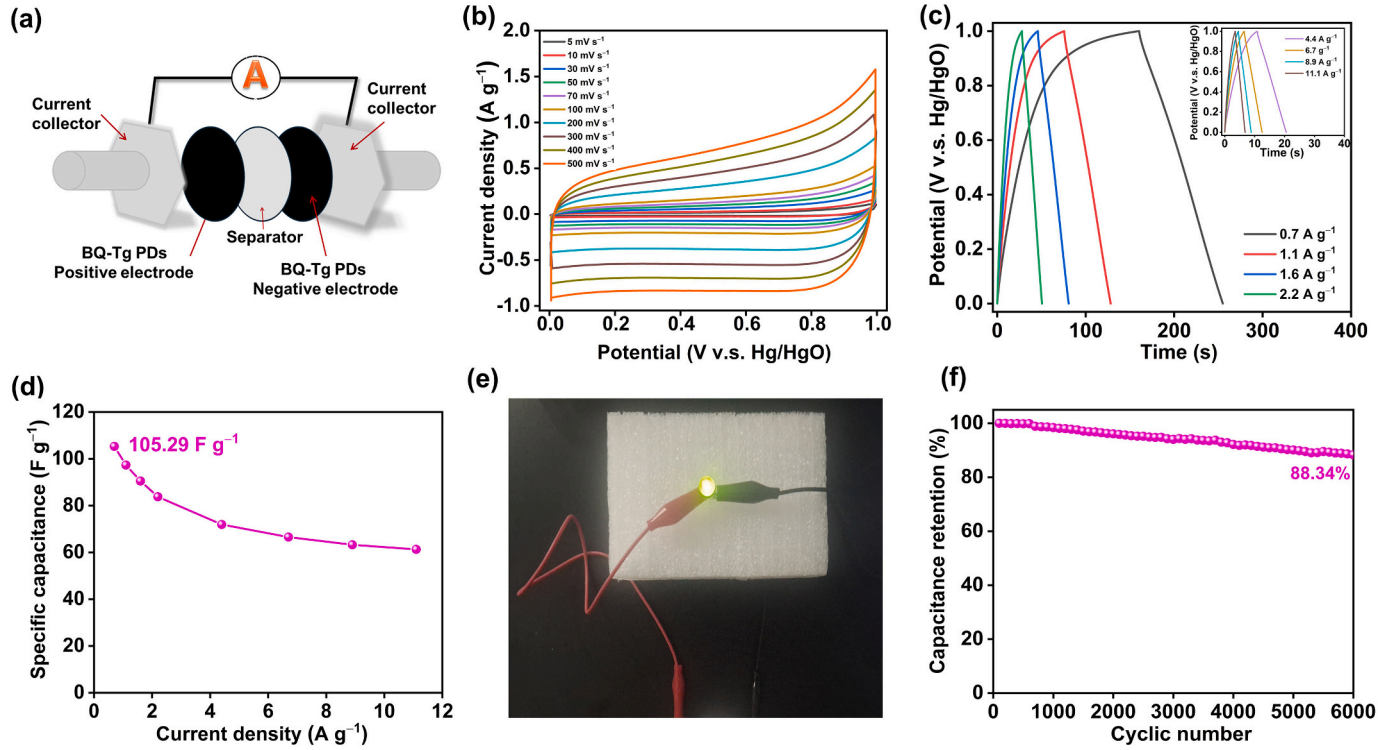

Fig. 7. (a) A model of the designed SSC device of the BQ-Tg PDs. (b) CV curves of the BQ-Tg PDs, (c) GCD curves of the BQ-Tg PDs, (d) Specific capacitances of the BQ-Tg PDs, (e) Photograph demonstrating the BQ-Tg PDs-based SSC device powering a green LED, confirming its practical real-world applicability, and (f) extending cycling efficiency over 6000 cycles tested at a current density of 2.2 A g^{-1} of the BQ-Tg PDs-based SSC device. (For interpretation of the references to colour in this figure legend, the reader is referred to the web version of this article.)

eq. (S5). The estimated capacitances were 105.29, 97.33, 90.48, 83.78, 71.93, 66.56, 63.26, and 61.3 F g^{-1} at current densities of 0.7, 1.1, 1.6, 2.2, 4.4, 6.7, 8.9, and 11.1 A g^{-1}, respectively (Fig. 7d), thereby validating the good efficacy of our supercapacitor apparatus. These capacitance values are also greater than those reported for symmetric supercapacitor devices and other configurations employing similar polymers (27–64 F g^{-1}) [11,91–93]. The differences in the CV and GCD profiles between the three-electrode supercapacitor (SC) test and the two-electrode symmetric supercapacitor (SSC) device mainly arise from the measurement configuration and the fact that the SSC records the full-cell response rather than an individual electrode. In the three-electrode setup, the potential of the working electrode is controlled against a reference electrode, so the recorded CV/GCD reflects the intrinsic behavior of a single electrode (including its pseudocapacitive/redox features) with minimal influence from the counter electrode [94]. In contrast, the two-electrode SSC measures the overall cell voltage, which is the sum of the potential changes at both electrodes together with polarization losses (solution/ohmic resistance, charge-transfer resistance, and mass-transport limitations) [94]. Moreover, the inclusion of a separator in the SSC system complicates measurements by obstructing direct electrode contact and elevating internal resistance, hence impacting ion transport and electrochemical stability [94]. As a result, redox/capacitive features that are distinct in the three-electrode configuration can become broadened, shifted, or partially masked in the SSC, and the GCD curves often show less ideal linearity due to the combined internal resistance of the device, including the separator and contact resistances [94]. Additionally, in a three-electrode supercapacitor setup, the mass loading of active material on the working electrode is 0.01 mg, facilitating optimal ion diffusion and precise electrochemical characterization. This minimal loading enables distinct, regular CV curves and almost linear galvanostatic charge-discharge (GCD) profiles [95,96]. Conversely, the SSC system uses 1.28 mg cm^{-2} per electrode to create realistic device conditions [97]. Increased mass loading elevates ion diffusion resistance, resulting in less ideal CV shapes in the GCD curves, which diminishes rate performance and lowers apparent capacitance [95]. Furthermore, the aggregation of active materials extends charge transport pathways and obstructs ion diffusion, hence impeding electrochemical kinetics and influencing performance [96]. Therefore, the apparent differences are expected and arise from the distinction between intrinsic single-electrode behavior (three-electrode) and practical full-device performance (two-electrode).

The Ragone plot (Fig. S20) emphasized the device's good performance, providing an energy density of 14.63 Wh kg^{-1} at a power density of 555.8 W kg^{-1}. As power density rises, energy density progressively decreases, illustrating the conflict between energy storage and rapid discharge capabilities. This behavior is characteristic of supercapacitors, wherein increased power output compromises stored energy. Moreover, as a proof-of-concept demonstration of practical applicability, three BQ-Tg PDs-based SSC devices connected in series were charged within a total voltage of 3.0 V and then directly connected to an external load. As shown in Fig. 7e, the charged device successfully powered a 1.8 V LED, which remained continuously illuminated for approximately 20 s. This simple test visually confirms that the BQ-PD-based SSC can efficiently store and deliver energy with a stable output, highlighting its promise for low-power, short-duration electronic applications. Fig. 7f illustrates the BQ-Tg PDs-based SC module's capacitance retention of 88.34% over 6000 cycles of charging and discharging at a current density of 2.2 A g^{-1}, demonstrating good circuit longevity and rate efficiency. The apparent decrease beyond extended cycling originates from the gradual accumulation of polarization and interfacial changes that are typical in full two-electrode devices. In particular, during long-term charge/discharge, (i) electrode/electrolyte interfacial resistance increases due to partial blockage of redox-active sites and slow restructuring of the electrode surface, (ii) repeated ion insertion/extraction can induce microstructural/packing changes within the thick electrode (higher mass loading in the SSC than in the three-electrode test), which lengthens ion-transport pathways and reduces utilization of active material at high cycle numbers, and (iii) contact resistance at the current collector/electrode and separator/electrode interfaces can progressively rise, increasing the IR drop and lowering the accessible capacitance [98–101]. These factors collectively lead to a moderate decline in capacitance after prolonged cycling, even though the overall retention remains acceptable (88.34% at 6000 cycles). To further verify the long-term electrode stability, the BQ-Tg PDs electrode was characterized before the 1st GCD (as-prepared) and after the 6000th GCD using FT-IR, XPS, XRD, and SEM (Figs. S21-S24). The FT-IR spectra preserve the characteristic N—H vibration (3570–3166 cm^{-1}) and the quinone C═O band (1622 cm^{-1}), suggesting that the chemical framework of the polymer dots is maintained during cycling (Fig. S21). Consistently, the XPS survey spectra display the same elemental signals (C 1 s, N 1 s, and O 1 s) before and after cycling without new impurity peaks, confirming stable surface composition (Fig. S22). In addition, the XRD patterns retain the broad amorphous feature, indicating no noticeable structural transformation (Fig. S23). The post-cycling SEM images show that no notable changes in the morphology of the material, with no obvious cracking, indicating good mechanical integrity after prolonged charge/discharge (Fig. S24). Collectively, these results demonstrate that the BQ-Tg PDs electrode exhibits excellent morphological and chemical stability, which underpins the good cycling durability of the SSC device.

4. Conclusions

In summary, we have successfully developed a novel class of benzoquinone-based polymer dots (BQ-PDs) through a simple one-step reaction between p-benzoquinone and aromatic diamines (Tg-2NH_2 and To-2NH_2). This direct synthetic strategy eliminates the need for conventional multi-step polymerization and nanoprecipitation, producing nanoscale redox-active polymer dots with well-integrated carbonyl functionalities. The resulting BQ-Tg and BQ-To PDs exhibit excellent thermal stability ($T_{d_{10}}$ = 387.04 °C and 380.95 °C, respectively), uniform nanoscale morphology (45–80 nm), and abundant electroactive sites that enhance charge transport and pseudocapacitive behavior. Electrochemical measurements revealed that BQ-Tg PDs achieved good specific capacitance of 268.8 F g^{-1} at 0.5 A g^{-1} in a three-electrode system, retaining 79.3% capacitance after 10,000 cycles. In a symmetric two-electrode device, BQ-Tg PDs delivered 105.29 F g^{-1} with 88.34% retention after 6000 cycles, alongside an energy density of 14.63 Wh kg^{-1} at a power density of 555.8 W kg^{-1}. These results establish BQ-based PDs as robust and efficient electrode materials for good-performance supercapacitors. Beyond energy storage, this versatile one-step design approach provides a general platform for engineering redox-active polymer dots, opening new opportunities in catalysis, sensing, and optoelectronic applications.

CRediT authorship contribution statement

Shimaa Abdelnaser: Validation, Methodology, Investigation, Conceptualization, Writing – original draft. **Yousra M. Nabil:** Investigation, Data curation, Conceptualization. **Hira Karim:** Software, Resources. **Shiao-Wei Kuo:** Resources, Project administration, Investigation, Funding acquisition. **Ahmed F.M. EL-Mahdy:** Validation, Resources, Project administration, Methodology, Investigation, Funding acquisition, Conceptualization, Writing – review & editing, Writing – original draft.

Declaration of competing interest

The authors declare that they have no recognized competing financial interests or personal connections that could have influenced the work presented in this study.

Acknowledgements

This study gained financial assistance from the National Science and Technology Council, Taiwan, under contract NSTC 112-2221-E-110-005-MY3 and 113-2218-E-110-004.

Appendix A. Supplementary data

Supplementary data to this article can be found online at https://doi.org/10.1016/j.cej.2026.173135.

Data availability

Data will be made available on request.

References

[1] Y. Luo, W. Zeng, Y. Wang, D. Li, X. Hu, H. Zhang, A hybrid approach for examining the drivers of energy consumption in Shanghai, Renew. Sust. Energ. Rev. 151 (2021) 111571, https://doi.org/10.1016/j.rser.2021.111571.
[2] A. Elkhatat, S. Al-Muhtaseb, Climate change and energy security: a comparative analysis of the role of energy policies in advancing environmental sustainability, Energies 17 (2024) 3179, https://doi.org/10.3390/en17133179.
[3] H.A. Khan, M. Tawalbeh, B. Aljawrneh, W. Abuwatfa, A. Al-Othman, H. Sadeghifar, A.G. Olabi, A comprehensive review on supercapacitors: their promise to flexibility, high temperature, materials, design, and challenges, Energy 295 (2024) 131043, https://doi.org/10.1016/j.energy.2024.131043.
[4] J. Mu, Y. Zhao, Z. Guo, Z. Zhang, H. Che, Y. Wang, X. Zhang, G. Wang, J. Mu, L. Wang, Rational design of new, efficient, and suitable nickel phthalocyanine reinforced MXene electrodes for supercapacitors, J. Energy Storage 61 (2023) 106768, https://doi.org/10.1016/j.est.2023.106768.
[5] Y. Zhao, Z. Feng, Z. Guo, J. Mu, H. Che, Z. Zhang, T. Tian, Z. Xiaoliang, S. Li, Y. Wang, J. Mu, Fe incorporated ternary layered double hydroxides with remarkably improved electrochemical performance towards asymmetric supercapacitors, Ceram. Int. 48 (2022) 27369–27378, https://doi.org/10.1016/j.ceramint.2022.05.213.
[6] S. Gokul Eswaran, M. Rashad, A. Santhana Krishna Kumar, A.F.M. EL-Mahdy, A comprehensive review of mxene-based emerging materials for energy storage applications and future perspectives, Chem. – An Asian J. 20 (2025) e202401181, https://doi.org/10.1002/asia.202401181.
[7] S. Abdelnaser, S.-W. Kuo, A.F.M. EL-Mahdy, Conjugated microporous polymers incorporating pyridine moieties for efficient faradaic supercapacitor energy storage, J. Power Sources 635 (2025) 236535, https://doi.org/10.1016/j.jpowsour.2025.236535.
[8] J. Zhan, A.F.M. EL-Mahdy, Redox-active Benzodithiophene-4, 8-dione-based conjugated microporous polymers for high-performance faradaic supercapacitor energy storage, Chem. Eng. J. 473 (2023) 145124, https://doi.org/10.1016/j.jpowsour.2025.236535.
[9] N. Parvin, M. Dhananjaya, M. Kang, S. Joo, J.H. Jung, T.K. Mandal, Recent advances in hybrid supercapacitors: a review of high performance materials and scalable fabrication techniques, J. Mater. Chem. A 13 (2025) 24320, https://doi.org/10.1039/d5ta02887f.
[10] S. Sharanappa, S.P. Vijaykumar, D.S. Suresh, A.B. Shbil, H. Ganesha, S. Veeresh, Y.S. Nagaraju, H. Devendrappa, Synthesis of water-soluble nitrogen doped carbon quantum dots-polypyrrole nanocomposite via in-situ polymerization for high performance supercapacitor application, J. Energy Storage 74 (2023) 109371, https://doi.org/10.1016/j.est.2023.109371.
[11] A.F. Saber, S. Abdelnaser, A.F.M. EL-Mahdy, S.-W. Kuo, One-pot synthesis of heteroatom-rich Anthraquinone-based Benzoxazine-linked porous organic polymers for high performance supercapacitors, Electrochim. Acta 511 (2025) 145397, https://doi.org/10.1016/j.electacta.2024.145397.
[12] H. Parsimehr, A. Ehsani, Algae-based electrochemical energy storage devices, Green Chem. 22 (2020) 8062–8096, https://doi.org/10.1039/d0gc02246b.
[13] X. Yang, T. Lv, J. Qiu, High mass-loading biomass-based porous carbon electrodes for supercapacitors: review and perspectives, Small 19 (2023) 2300336, https://doi.org/10.1002/smll.202300336.
[14] R. Aslani, F. Alimola, N. Arsalani, Fabrication of a new hyperbranched polymer for the preparation of a polymer dot as a supercapacitor with enhanced electrochemical performance, J. Alloys Compd. 1033 (2025) 181190, https://doi.org/10.1016/j.jallcom.2025.181190.
[15] Y. Wu, C. Shi, G. Wang, H. Sun, S. Yin, Recent advances in the development and applications of conjugated polymer dots, J. Mater. Chem. B 10 (2022) 2995–3015, https://doi.org/10.1039/d1tb02816b.
[16] Y. Yuan, W. Hou, W. Qin, C. Wu, Recent advances in semiconducting polymer dots as optical probes for biosensing, Biomater. Sci. 9 (2021) 328–346, https://doi.org/10.1039/d0bm01038c.
[17] S.-X. Liao, A.F.M. EL-Mahdy, Redox-active conjugated microporous polymers featuring a precise pore size for high-performance supercapacitor energy storage, ACS Appl. Energy Mater. 8 (2025) 3074–3086, https://doi.org/10.1021/acsaem.4c03232.
[18] S. Abdelnaser, S.-W. Kuo, A.F.M. EL-Mahdy, Conjugated anthraquinone-linked microporous polymers with enhanced energy storage performance, J. Power Sources 658 (2025) 238225, https://doi.org/10.1016/j.jpowsour.2025.238225.
[19] B. Sun, B. Zhao, D. Wang, Y. Wang, Q. Tang, S. Zhu, B. Yang, H. Sun, Fluorescent non-conjugated polymer dots for targeted cell imaging, Nanoscale 8 (2016) 9837–9841, https://doi.org/10.1039/c6nr01909a.
[20] B.R. Babu, R. Sasikumar, M. Arivanandhan, R. Jayavel, Functionalised carbon fiber based flexible symmetric supercapacitors with wider potential window for sustainable energy storage applications, J. Power Sources 625 (2025) 235727, https://doi.org/10.1016/j.jpowsour.2024.235727.
[21] Y.K. Kim, J.E. Lee, B. Ryplida, C.A. Choi, Z.A.I. Mazrad, G. Lee, S. Lee, I. In, J. H. Jeong, S.Y. Park, Redox-responsive FRET-based polymer dot with BODIPY for fluorescence imaging-guided chemotherapy of tumor, Eur. J. Pharm. Biopharm. 132 (2018) 200–210, https://doi.org/10.1016/j.ejpb.2018.09.025.
[22] Z. Huang, Y. Wu, C. Yu, Z. Wang, C. Jin, Z. Li, S. Yin, Impact of the donor–acceptor structure on photocatalytic hydrogen generation by polyfluorene polymer dots, ACS Appl. Polym. Mater. 7 (2025) 3399–3408, https://doi.org/10.1021/acsapm.5c00214.
[23] J. Guo, X. Wei, Y. Liu, Y. Li, P.C. Ke, Z. Yuan, Biomimetic semiconducting polymer dots for dual targeted NIR-II phototheranostic and multimodal coordinated immunostimulatory therapy, J. Mater. Chem. B 13 (2025) 12234–12245, https://doi.org/10.1039/d5tb00976f.
[24] C.-L. Chang, W.-C. Lin, C.-Y. Jia, L.-Y. Ting, J. Jayakumar, M.H. Elsayed, Y.-Q. Yang, Y.-H. Chan, W.-S. Wang, C.-Y. Lu, Low-toxic cycloplatinated polymer dots with rational design of acceptor co-monomers for enhanced photocatalytic efficiency and stability, Appl. Catal. B Environ. 268 (2020) 118436, https://doi.org/10.1016/j.apcatb.2019.118436.
[25] M.G. Kotp, N.L. Torad, J. Lüder, A.A.M. El-Amir, W. Chaikittisilp, Y. Yamauchi, A. F.M. EL-Mahdy, A phenazine-conjugated microporous polymer-based quartz crystal microbalance for sensitive detection of formaldehyde vapors at room temperature: an experiment and density functional theory study, J. Mater. Chem. A 11 (2023) 764–774, https://doi.org/10.1039/d2ta07966f.
[26] D. Huang, Y. Chen, M. Cheng, L. Lei, S. Chen, W. Wang, X. Liu, Carbon dots-decorated carbon-based metal-free catalysts for electrochemical energy storage, Small 17 (2021) 2002998, https://doi.org/10.1002/smll.202002998.
[27] A.F.M. EL-Mahdy, J. Lüder, M.G. Kotp, S.-W. Kuo, A Tröger's base-derived covalent organic polymer containing carbazole units as a high-performance supercapacitor, Polymers 13 (2021) 1385, https://doi.org/10.3390/polym13091385.
[28] S. Ghosh, S. Barg, S.M. Jeong, K. Ostrikov, Heteroatom-doped and oxygen-functionalized nanocarbons for high-performance supercapacitors, Adv. Energy Mater. 10 (2020) 2001239, https://doi.org/10.1002/aenm.202001239.
[29] A. Rayar, S. Chapi, M.V. Murugendrappa, G. Babaladimath, K.N. Harish, R. R. Kakarla, A.V. Raghu, Organic conjugated polymers and their nanostructured composites: synthesis methodologies and electrochemical applications, Nano-Struct. Nano-Objects 37 (2024) 101102, https://doi.org/10.1016/j.nanoso.2024.101102.
[30] M. Carta, M. Croad, K. Bugler, K.J. Msayib, N.B. McKeown, Heterogeneous organocatalysts composed of microporous polymer networks assembled by Tröger's base formation, Polym. Chem. 5 (2014) 5262–5266, https://doi.org/10.1039/c4py00608a.
[31] Y. Cui, J. Du, Y. Liu, Y. Yu, S. Wang, H. Pang, Z. Liang, J. Yu, Design and synthesis of a multifunctional porous N-rich polymer containing: S -triazine and Tröger's base for CO_2 adsorption, catalysis and sensing, Polym. Chem. 9 (2018) 2643–2649, https://doi.org/10.1039/c8py00177d.
[32] Y. Cui, Y. Liu, J. Liu, J. Du, Y. Yu, S. Wang, Z. Liang, J. Yu, Multifunctional porous Tröger's base polymers with tetraphenylethene units: CO2 adsorption, luminescence and sensing properties, Polym. Chem. 8 (2017) 4842–4848, https://doi.org/10.1039/c7py00856b.
[33] Z. Yang, H. Zhang, B. Yu, Y. Zhao, G. Ji, Z. Liu, Tröger's base-derived microporous organic polymer : design and applications in CO_2 / H_2 capture and CO_2 hydrogenation into formic acid, Chem. Commun. 51 (2015) 1271–1274, https://doi.org/10.1039/c4cc08295h.
[34] M. Ahmed, A.F.M. EL-Mahdy, Multistep continuous synthesis of a highly fluorescent Tröger's base-derived Benzoxazine: its thermal conversion into intrinsic microporosity polymers, Macromolecules 57 (2024) 5472–5485, https://doi.org/10.1021/acs.macromol.3c02657.
[35] M. Carta, R. Malpass-Evans, M. Croad, Y. Rogan, J.C. Jansen, P. Bernardo, F. Bazzarelli, N.B. McKeown, An efficient polymer molecular sieve for membrane gas separations, Science 339 (2013) 303–307, https://doi.org/10.1126/science.1228032.
[36] R. Williams, L.A. Burt, E. Esposito, J.C. Jansen, E. Tocci, C. Rizzuto, M. Lanč, M. Carta, N.B. McKeown, A highly rigid and gas selective methanopentacene-based polymer of intrinsic microporosity derived from Tröger's base polymerization, J. Mater. Chem. A 6 (2018) 5661–5667, https://doi.org/10.1039/c8ta00509e.
[37] Z.G. Wang, X. Liu, D. Wang, J. Jin, Tröger's base-based copolymers with intrinsic microporosity for CO_2 separation and effect of Tröger's base on separation performance, Polym. Chem. 5 (2014) 2793–2800, https://doi.org/10.1039/c3py01608k.
[38] M. Lee, C.G. Bezzu, M. Carta, P. Bernardo, G. Clarizia, J.C. Jansen, N. B. McKeown, Enhancing the gas permeability of Tröger's base derived polyimides of intrinsic microporosity, Macromolecules 49 (2016) 4147–4154, https://doi.org/10.1021/acs.macromol.6b00351.
[39] J.W. Jeon, J. Shin, J. Lee, J.H. Baik, R. Malpass-Evans, N.B. McKeown, T.H. Kim, J.C. Lee, S.K. Kim, B.G. Kim, Hierarchically structured carbon electrodes derived

from intrinsically microporous Tröger's base polymers for high-performance supercapacitors, Appl. Surf. Sci. 530 (2020) 147146, https://doi.org/10.1016/j.apsusc.2020.147146.
[40] S.D. Jagadale, S.V. Bhosale, High-performance flexible symmetric supercapacitor device based on Nitroaniline-functionalized benzoquinone, ACS Appl. Energy Mater. 2024 (7) (2024) 10921–10937, https://doi.org/10.1021/acsaem.4c01762.
[41] C. Meng, N. An, S. Song, L. Wang, L. Xiao, Y. Zhou, R. Qiang, Y. Yang, Z. Li, Z. Hu, Accurate prediction of redox potential and the rational design of organic molecular electrode with multi-electron active centers for supercapacitor, J. Power Sources 102 (2024) 114122, https://doi.org/10.1016/j.est.2024.114122.
[42] J.Y. Kim, J.-W. Ho, D. Kim, M.-W. Moon, G.H. Choi, P.J. Yoo, Unveiling dominant impact of electrochemical stability on performance deterioration in alkaline redox flow batteries utilizing different benzoquinone derivatives, J. Power Sources 611 (2024) 234766, https://doi.org/10.1016/j.jpowsour.2024.234766.
[43] J. Yang, P. Shao, X. Zhao, Y. Liao, C. Yan, Quinone-amine polymer nanospheres with enhanced redox activity for aqueous proton storage, J. Colloid Interface Sci. 650 (2023) 1811–1820, https://doi.org/10.1016/j.jcis.2023.07.106.
[44] J. Liang, Y. Hou, Y. You, L. Dong, B. Mei, H. Niu, Quinone-amine polymers prepared by simple precipitation polymerization and used as cathodes for aqueous zinc-ion batteries and electrochromic materials, J. Mater. Chem. C 12 (2024) 4655, https://doi.org/10.1039/d4tc00474d.
[45] W. Cai, Z. Wang, Z. Shu, W. Liu, J. Wang, J. Qiu, Development of a fully bio-based hyperbranched benzoxazine, Polym. Chem. 12 (2021) 6894–6902, https://doi.org/10.1039/d1py01451j.
[46] E.V. Nosova, G.N. Lipunova, G.V. Zyryanov, V.N. Charushin, O.N. Chupakhin, Functionalized 1,3,5-triazine derivatives as components for photo- and electroluminescent materials, Org. Chem. Front. 9 (2022) 6646–6683, https://doi.org/10.1039/d2qo00961g.
[47] J. Dai, G. Li, Y. Hu, L. Han, Hollow carbon spheres anchored with nitrogen-doped carbon dots for high-performance supercapacitors, J. Energy Storage 83 (2024) 110640, https://doi.org/10.1016/j.est.2024.110640.
[48] H. Quan, W. Tao, Y. Wang, D. Chen, Enhanced supercapacitor performance of Camellia oleifera shell derived hierarchical porous carbon by carbon quantum dots, J. Energy Storage 55 (2022) 105573, https://doi.org/10.1016/j.est.2022.105573.
[49] T.-L. Yang, J.-Y. Chen, S.-W. Kuo, C.-T. Lo, A.F.M. EL-Mahdy, Hydroxyl-functionalized covalent organic frameworks as high-performance supercapacitors, Polymers 14 (2022) 3428, https://doi.org/10.3390/polym14163428.
[50] S.S. Shah, M.A. Aziz, Properties of electrode materials and electrolytes in supercapacitor technology, J. Chem. Environ. 3 (2024) 1–45, https://doi.org/10.56946/jce.v3i1.309.
[51] W. Liu, M. Ulaganathan, I. Abdelwahab, X. Luo, Z. Chen, S.J. Rong Tan, X. Wang, Y. Liu, D. Geng, Y. Bao, Two-dimensional polymer synthesized via solid-state polymerization for high-performance supercapacitors, ACS Nano 12 (2018) 852–860, https://doi.org/10.1021/acsnano.7b08354.
[52] K.J. Aoki, J. Chen, Y. Liu, B. Jia, Peak potential shift of fast cyclic voltammograms owing to capacitance of redox reactions, J. Electroanal. Chem. 856 (2020) 113609, https://doi.org/10.1016/j.jelechem.2019.113609.
[53] T.T.T. Vuong, V.V. Thang, T.N. Tran, N.M. Hieu, P.L. Nguyen, T.V.B. Phung, High-performance supercapacitors from composites derived from recycled alkaline batteries, Sci. Rep. 15 (2025) 41600, https://doi.org/10.1038/s41598-025-25571-7.
[54] D.A. Bograchev, Y.M. Volfkovich, S. Martemianov, Diagnostics of supercapacitors using cyclic voltammetry: modeling and experimental applications, J. Electroanal. Chem. 935 (2023) 117322, https://doi.org/10.1016/j.jelechem.2023.117322.
[55] Q. Tayyaba, N. Sultan, S. Siddique, A. Khan, Insights into the electrochemical performance of manganese dioxide coated metallic foils as potential electrodes for supercapacitors, J. Appl. Electrochem. 55 (2025) 905–917, https://doi.org/10.1007/s10800-024-02211-y.
[56] C. Cougnon, Impact of the scan rate on the stability window of an electrical double-layer capacitor, Energies 16 (2023) 5687, https://doi.org/10.3390/en16155687.
[57] C. Fan, Y. Dong, Y. Liu, L. Zhang, D. Wang, X. Lin, Y. Lv, S. Zhang, H. Song, D. Jia, Mesopore-dominated hollow carbon nanoparticles prepared by simple air oxidation of carbon black for high mass loading supercapacitors, Carbon 160 (2020) 328–334, https://doi.org/10.1016/j.carbon.2020.01.034.
[58] I. Hussain, K. Singh, A.C. Mendhe, M.R. Thalji, S. Mandal, I. Ali, A.F.M. EL-Mahdy, P. Rosaiah, M.K. Aslam, T.L. Tamang, Integration of non-Ti_3C_2 MXene with carbon-based materials for energy storage devices: recent advancements and future aspects, Prog. Solid State Chem. 78 (2025) 100523, https://doi.org/10.1016/j.progsolidstchem.2025.100523.
[59] H. Sun, Z. Ullah, L. Chen, W. Li, H. Chen, X. Guan, X. An, M. Chen, L. Liu, Q. Li, Photo-assisted liquid organic cathode with ultralow resistance and high diffusion coefficient for membrane-free aqueous zinc-ion battery, Adv. Energy Mater. 15 (2025) 2501115, https://doi.org/10.1002/aenm.202501115.
[60] A.F. Saber, S.U. Sharma, J.-T. Lee, A.F.M. EL-Mahdy, S.-W. Kuo, Carbazole-conjugated microporous polymers from Suzuki–Miyaura coupling for supercapacitors, Polymer 254 (2022) 125070, https://doi.org/10.1016/j.polymer.2022.125070.
[61] A.F.M. EL-Mahdy, T.C. Yu, S.-W. Kuo, Synthesis of multiple heteroatom–doped mesoporous carbon/silica composites for supercapacitors, Chem. Eng. J. 414 (2021) 128796, https://doi.org/10.1016/j.cej.2021.128796.
[62] M.M. Samy, M.G. Mohamed, A.F.M. EL-Mahdy, T.H. Mansoure, K.C.-W. Wu, S.-W. Kuo, High-performance supercapacitor electrodes prepared from dispersions of tetrabenzonaphthalene-based conjugated microporous polymers and carbon nanotubes, ACS Appl. Mater. Interfaces 13 (2021) 51906–51916, https://doi.org/10.1021/acsami.1c05720.
[63] G.V. Vijayaraghavan, R. Suriakarthick, J. Priscilla, T.S. Shyju, J. Mani, Electrical, electrochemical and thermoelectric properties of PANI/$AgBiSe_2$ multi-functional polymeric composite material for energy storage and conversion applications, J. Alloys Compd. 1021 (2025) 179534, https://doi.org/10.1016/j.jallcom.2025.179534.
[64] M.G. Mohamed, S.U. Sharma, P.-T. Wang, M. Ibrahim, M.-H. Lin, C.-L. Liu, M. Ejaz, H.-J. Yen, S.-W. Kuo, Construction of fully π-conjugated, diyne-linked conjugated microporous polymers based on tetraphenylethene and dibenzo [g, p] chrysene units for energy storage, Polym. Chem. 15 (2024) 2827–2839, https://doi.org/10.1039/d4py00421c.
[65] M.G. Mohamed, C.-C. Chen, M. Ibrahim, A. Osama Mousa, M.H. Elsayed, Y. Ye, S.-W. Kuo, Tetraphenylanthraquinone and Dihydroxybenzene-tethered conjugated microporous polymer for enhanced CO_2 uptake and Supercapacitive energy storage, JACS Au 4 (2024) 3593–3605, https://doi.org/10.1021/jacsau.4c00537.
[66] M.G. Mohamed, H.-Y. Hu, S. Santhoshkumar, M. Madhu, T.H. Mansoure, C.-W. Hsiao, Y. Ye, C.-W. Huang, W.-L. Tseng, S.-W. Kuo, Design and synthesis of bifunctional conjugated microporous polymers containing tetraphenylethene and bisulfone units for energy storage and fluorescent sensing of p-nitrophenol, Coll. Surf. A Physicochem. Eng. Asp. 680 (2024) 132675, https://doi.org/10.1016/j.colsurfa.2023.132675.
[67] S.U. Sharma, M.H. Elsayed, I.M.A. Mekhemer, T.S. Meng, H.H. Chou, S.W. Kuo, M.G. Mohamed, Rational design of pyrene and thienyltriazine-based conjugated microporous polymers for high-performance energy storage and visible-light photocatalytic hydrogen evolution from water, Giant 17 (2024) 100217, https://doi.org/10.1016/j.giant.2023.100217.
[68] J. Dong, S. Li, Y. Ding, Anchoring nickel-cobalt sulfide nanoparticles on carbon aerogel derived from waste watermelon rind for high-performance asymmetric supercapacitors, J. Alloys Compd. 845 (2020) 155701, https://doi.org/10.1016/j.jallcom.2020.155701.
[69] T. He, Z. Wang, X. Li, Y. Tan, Y. Liu, L. Kong, L. Kang, C. Chen, F. Ran, Intercalation structure of vanadium nitride nanoparticles growing on graphene surface toward high negative active material for supercapacitor utilization, J. Alloys Compd. 781 (2019) 1054–1058, https://doi.org/10.1016/j.jallcom.2018.12.149.
[70] M. Wang, J. Zhang, X. Yi, B. Liu, X. Zhao, X. Liu, High-performance asymmetric supercapacitor made of $NiMoO_4$ nanorods@Co_3O_4 on a cellulose-based carbon aerogel, Beilstein J. Nanotechnol. 11 (2020) 240–251, https://doi.org/10.3762/bjnano.11.18.
[71] D. Wu, Y. Liu, Y. Wu, B. Tan, Z. Xie, Microporous carbons derived from organosilica-containing carbon dots with outstanding supercapacitance, Dalton Trans. 47 (2018) 5961–5967, https://doi.org/10.1039/c8dt00484f.
[72] E. Regulska, J. Breczko, A. Basa, B. Szydlowska, K. Kakareko, A. Rydzewska-Rosołowska, T. Hryszko, Graphene-quantum-dots-decorated $NiAl_2O_4$ nanostructure as supercapacitor and electrocatalyst in biosensing, Mater. Today Commun. 33 (2022) 104166, https://doi.org/10.1016/j.mtcomm.2022.104166.
[73] J. Zhu, L. Wang, X. Gan, T. Tang, F. Qin, W. Luo, Q. Li, N. Guo, S. Zhang, D. Jia, H. Song, Graphene quantum dot inlaid carbon nanofibers: revealing the edge activity for ultrahigh rate pseudocapacitive energy storage, Energy Storage Mater. 47 (2022) 158–166, https://doi.org/10.1016/j.ensm.2022.02.015.
[74] J. Huang, C. Liu, Y. Jin, J. Chen, Hierarchical porous carbon synthesis by carbonized polymer dots-based sacrificial template for high-performance supercapacitors, Chem. Eng. J. 461 (2023) 141930, https://doi.org/10.1016/j.cej.2023.141930.
[75] T.A. Gaber, L.R. Ahmed, A.F.M. EL-Mahdy, Efficient faradaic supercapacitor energy storage using redox-active pyrene-and benzodithiophene-4, 8-dione-tethered conjugated microporous polymers, J. Mater. Chem. A 11 (2023) 19408–19417, https://doi.org/10.1039/d3ta03198e.
[76] A. Patel, S.K. Patel, R.S. Singh, R.P. Patel, Review on recent advancements in the role of electrolytes and electrode materials on supercapacitor performances, Discov. Nano 19 (2024) 188, https://doi.org/10.1186/s11671-024-04053-1.
[77] M.R. Islam, S. Afroj, N. Karim, Scalable production of 2D material Heterostructure textiles for high-performance wearable supercapacitors, ACS Nano 17 (2023) 18481–18493, https://doi.org/10.1021/acsnano.3c06181.
[78] C.G. Cannon, P.A.A. Klusener, N.P. Brandon, A.R.J. Kucernak, Aqueous redox flow batteries: small organic molecules for the positive electrolyte species, ChemSusChem 16 (2023) e202300303, https://doi.org/10.1002/cssc.202300303.
[79] K. Surya, M.S. Michael, Novel interconnected hierarchical porous carbon electrodes derived from bio-waste of corn husk for supercapacitor applications, J. Electroanal. Chem. 878 (2020) 114674, https://doi.org/10.1016/j.jelechem.2020.114674.
[80] T. Chen, Z. Liu, Starch-assistant synthesis of Ni quantum dots/ultrathin carbon nanosheet hybrids for high performance supercapacitor, Mater. Lett. 236 (2019) 248–251, https://doi.org/10.1016/j.matlet.2018.10.114.
[81] X. Li, J. Rong, B. Wei, Electrochemical behavior of single-walled carbon nanotube supercapacitors under compressive stress, ACS Nano 4 (2010) 6039–6049, https://doi.org/10.1021/nn101595y.
[82] Y. Lian, Z. Xu, D. Wang, Y. Bai, C. Ban, J. Zhao, H. Zhang, Nb_2O_5 quantum dots coated with biomass carbon for ultra-stable lithium-ion supercapacitors, J. Alloys Compd. 850 (2021) 156808, https://doi.org/10.1016/j.jallcom.2020.156808.

[83] J.H. Wang, A.E. Hassan, A.M. Elewa, A.F.M. EL-Mahdy, Donor–acceptor hetero [6] radialene-based three-dimensional covalent organic frameworks for organic pollutant adsorption, photocatalytic degradation, and hydrogen production activity, J. Mater. Chem. A 12 (2024) 14005–14021, https://doi.org/10.1039/d3ta07691a.
[84] A.I. Al-Sulami, N.Y. Elamin, E. Aldosari, M.O. Farea, S.S. Alzahrani, A.M. Al-Harthi, E.M. Alharbi, A. Rajeh, Tunable band gap and ionic conductivity in PMMA and PANI blend with WO_3 nanocomposites for optoelectronics and energy storage devices, Sci. Rep. 15 (2025) 34543, https://doi.org/10.1038/s41598-025-17880-8.
[85] V.S. Bhat, A. Toghan, G. Hegde, R.S. Varma, Capacitive dominated charge storage in supermicropores of self-activated carbon electrodes for symmetric supercapacitors, J. Energy Storage 52 (2022) 104776, https://doi.org/10.1016/j.est.2022.104776.
[86] Y. Liu, L. Zhou, J. Ouyang, X. Ao, M. Shuang, A.A. Adesina, Electrodeposition nanofabrication of carboxylated carbon nanotubes/α-MnO_2 nanorods/polypyrrole composites as high hybrid capacitance electrodes for efficient U (VI) electrosorption, Sep. Purif. Technol. 334 (2024) 125989, https://doi.org/10.1016/j.seppur.2023.125989.
[87] A. Toghan, M. Khairy, E.M. Kamar, M.A. Mousa, Effect of particle size and morphological structure on the physical properties of $NiFe_2O_4$ for supercapacitor application, J. Mater. Res. Technol. 19 (2022) 3521–3535, https://doi.org/10.1016/j.jmrt.2022.06.095.
[88] A.S. Raikwar, H.S. Panda, A review on nano-structured electrodes for high-performance supercapacitors : panoramic insights across dimensional spectra, Discov. Electron. 2 (2025) 2–94, https://doi.org/10.1007/s44291-025-00132-4.
[89] D. Kim, J. Park, S. Jung, J. Jang, M. Han, M. Kim, W. Zhu, W. Song, Y. Yamauchi, J. Kim, Nanoscale study on the importance of uniformity and nanoparticle size in ZIF-8 carbon nanoarchitecture for enhancing electrochemical properties, Nanoscale 17 (2025) 10344–10355, https://doi.org/10.1039/d5nr00556f.
[90] A. Nayak, B. Bhushan, S. Kotnala, N. Kukretee, P. Chaudhary, A.R. Tripathy, K. Ghai, S. Laxmi Mudliar, Nanomaterials for supercapacitors as energy storage application: focus on its characteristics and limitations, Mater. Today Proc. 73 (2023) 227–232, https://doi.org/10.1016/j.matpr.2022.11.259.
[91] S. Ravuri, A. Al-Othman, S. Al-Asheh, P. Nancarrow, K. Singh, M. Al-Sayah, Tuning the electrochemical potential window of niobium carbide based electrodes for symmetric electrochemical supercapacitors, Case Stud. Chem. Environ. Eng. 10 (2024) 100812, https://doi.org/10.1016/j.cscee.2024.100812.
[92] A. Philip, A.R. Kumar, R.K. Edathil, An aqueous symmetric supercapacitor with wide window and high energy density using redox electrode of cu–Al-layered double hydroxides and λ-manganese dioxide, Environ. Sci. Pollut. Res. 31 (2024) 45295–45309, https://doi.org/10.1007/s11356-024-34138-4.
[93] V.V. Mohan, P.M. Anjana, R.B. Rakhi, One pot synthesis of tungsten oxide nanomaterial and application in the field of flexible symmetric supercapacitor energy storage device, Mater. Today Proc. 62 (2022) 848–851, https://doi.org/10.1016/j.matpr.2022.04.046.
[94] S. Sharma, P. Chand, Results in chemistry supercapacitor and electrochemical techniques : a brief review, Results Chem. 5 (2023) 100885, https://doi.org/10.1016/j.rechem.2023.100885.
[95] W. Li, M. Wu, W. Yang, M. Zhao, X. Lu, Electrochimica Acta effects of electrode mass loading on the self-discharge of supercapacitors, Electrochim. Acta 438 (2023) 141550, https://doi.org/10.1016/j.electacta.2022.141550.
[96] P. Xu, S. Luo, J. Liang, D. Pan, B. Zou, J. Li, High-performance 2.2 V asymmetric supercapacitors achieved by appropriate charge matching between ultrahigh mass-loading Mn_3O_4 and sodium-Jarosite derived FeOOH, Adv. Funct. Mater. 34 (2024) 2313927, https://doi.org/10.1002/adfm.202313927.
[97] T.K. Shivasharma, R. Sahu, M. Thosare, D. Sarker, U. Deshpande, B.R. Sankapal, Device grade solid-state pouch and coin cell supercapacitors dual assembly using consumed battery waste to best utilization, Sci. Rep. 15 (2025) 28406, https://doi.org/10.1038/s41598-025-96426-4 1.
[98] S.S. Karade, S. Lalwani, J. Eum, H. Kim, Coin cell fabricated symmetric supercapacitor device of two-steps synthesized V_2O_5 Nanorods, J. Electroanal. Chem. 864 (2020) 114080, https://doi.org/10.1016/j.jelechem.2020.114080.
[99] X. Chen, Q. Su, J. Yu, M. Wei, G. Guo, Y. Wang, Experimental study on the degradation mechanism of $LaCoO_3$-based symmetric supercapacitors, RSC Adv. 11 (2021) 25170–25178, https://doi.org/10.1039/d1ra03362j.
[100] E. Pameté, L. Köps, F.A. Kreth, S. Pohlmann, A. Varzi, T. Brousse, A. Balducci, V. Presser, The many deaths of supercapacitors: degradation, aging, and performance fading, Adv. Energy Mater. 13 (2023) 2301008, https://doi.org/10.1002/aenm.202301008.
[101] A.M.H.S. Panda, A review on electrolytes for supercapacitor device, Discov. Mater. 3 (2023) 3–29, https://doi.org/10.1007/s43939-023-00065-3.